

Hurricane Irene Sensitivity to Stratified Coastal Ocean Cooling

GREG SEROKA AND TRAVIS MILES

Center for Ocean Observing Leadership, Department of Marine and Coastal Sciences, School of Environmental and Biological Sciences, Rutgers, The State University of New Jersey, New Brunswick, New Jersey

YI XU

State Key Laboratory of Estuarine and Coastal Research, East China Normal University, Shanghai, China

JOSH KOHUT, OSCAR SCHOFIELD, AND SCOTT GLENN

Center for Ocean Observing Leadership, Department of Marine and Coastal Sciences, School of Environmental and Biological Sciences, Rutgers, The State University of New Jersey, New Brunswick, New Jersey

(Manuscript received 29 December 2015, in final form 25 April 2016)

ABSTRACT


Cold wakes left behind by tropical cyclones (TCs) have been documented since the 1940s. Many questions remain, however, regarding the details of the processes creating these cold wakes and their in-storm feedbacks onto tropical cyclone intensity. This largely reflects a paucity of measurements within the ocean, especially during storms. Moreover, the bulk of TC research efforts have investigated deep ocean processes—where tropical cyclones spend the vast majority of their lifetimes—and very little attention has been paid to coastal ocean processes despite their critical importance to shoreline populations. Using Hurricane Irene (2011) as a case study, the impact of the cooling of a stratified coastal ocean on storm intensity, size, and structure is quantified. Significant ahead-of-eye-center cooling (at least 6°C) of the Mid-Atlantic Bight occurred as a result of coastal baroclinic processes, and operational satellite SST products and existing coupled ocean–atmosphere hurricane models did not capture this cooling. Irene’s sensitivity to the cooling is tested, and its intensity is found to be most sensitive to the cooling over all other tested WRF parameters. Further, including the cooling in atmospheric modeling mitigated the high storm intensity bias in predictions. Finally, it is shown that this cooling—not track, wind shear, or dry air intrusion—was the key missing contribution in modeling Irene’s rapid decay prior to New Jersey landfall. Rapid and significant intensity changes just before landfall can have substantial implications on storm impacts—wind damage, storm surge, and inland flooding—and thus, coastal ocean processes must be resolved in future hurricane models.

1. Introduction

While tropical cyclone (TC) track prediction has steadily improved over the past two decades, TC intensity prediction has failed to progress in a similarly substantial way (Cangialosi and Franklin 2013). Many environmental factors control TC intensity, including the storm track

itself, wind shear, intrusion of dry air, and upper-ocean thermal evolution (Emanuel et al. 2004). The last factor underlies all other processes because it directly impacts the fundamental transfer of energy from the ocean to the atmosphere within the TC heat engine (Emanuel 1999; Schade and Emanuel 1999).

Hurricane models often account for track and large-scale atmospheric processes that affect intensity—wind shear, dry air intrusion, and interaction with midlatitude troughs (Emanuel et al. 2004). Some possible reasons include (i) greater attention to the atmosphere in modeling, and (ii) large-scale processes being resolved well, even with less advanced models. However, models do a comparatively less accurate job of representing oceanic processes that govern hurricane intensity because

 Denotes Open Access content.

Corresponding author address: G. S. Seroka, Center for Ocean Observing Leadership, Department of Marine and Coastal Sciences, School of Environmental and Biological Sciences, Rutgers, The State University of New Jersey, New Brunswick, NJ 08901.
E-mail: greg.seroka@gmail.com

DOI: 10.1175/MWR-D-15-0452.1

they are data limited (Emanuel 1999, 2003; Emanuel et al. 2004).

A specific upper-ocean thermal phenomenon that consistently emerges after a TC has passed is a cold pool of water left in the wake of its path, termed a “cold wake.” This oceanic phenomenon has been observed behind TCs since at least the 1940s off the coast of Japan (Suda 1943) and since at least the 1950s in the Atlantic, Caribbean, and Gulf of Mexico (Fisher 1958). Observational studies continued into the 1960s (e.g., Leipper 1967) with investigation of potential processes causing the cold wakes, such as upwelling and turbulent entrainment of cold water into the warmer mixed layer. Studies in the late 1970s (Chang and Anthes 1979; Sutyryn and Agrenich 1979) began the use of idealized numerical simulations to investigate the effect of this oceanic cooling on TC intensity, but neglected TC movement. Then, numerical modeling studies in the 1980s (Price 1981; Sutyryn and Khain 1984) and 1990s (Khain and Ginis 1991; Bender et al. 1993; Price et al. 1994) incorporated TC movement and three-dimensional coupled ocean–atmosphere models to further examine the negative SST feedback on storm intensity.

Prior to the 1980s and 1990s, observations of the upper ocean beneath a TC were uncommon due to the unpredictable and dangerous winds, waves, and currents in the storms (D’Asaro 2003). At that point, ocean observations in TCs, summarized by Price (1981), occurred primarily as a result of targeted studies using air-deployed profilers (e.g., Sanford et al. 1987; Shay et al. 1992), long-term observations that happened to be close to a TC’s track (e.g., Forristall et al. 1977; Mayer and Mofjeld 1981; Dickey et al. 1998) or hydrographic surveys in a TC’s wake (e.g., Brooks 1983). The severe conditions of TCs hampered progress in determining physical processes leading to the previously observed cold wake, as well as specific timing and location of the ocean cooling relative to the TC core. In the 2000s, studies began to provide observational and model evidence that significant portions of this surface ocean cooling can occur ahead of the hurricane eye center (e.g., D’Asaro 2003; Jacob and Shay 2003; Jaimes and Shay 2009), proposing that such cooling is especially important for hurricane intensity.

Even today, the bulk of research efforts have investigated deep ocean processes and their feedback onto TC intensity; indeed, a TC typically spends the vast majority of its lifetime over deep, open waters. However, rapid and significant changes in intensity just before landfall and often in shallow water can have substantial implications on storm impacts (i.e., wind damage, storm surge, and inland flooding). For example, the statistical analysis by Rappaport et al. (2010) finds

that category-3–5 hurricanes in the Gulf of Mexico weakened approaching landfall due to both vertical wind shear and hurricane-induced sea surface temperature reductions on the order of 1°C ahead of the storm center. Therefore, attention must be paid to coastal processes as well (Marks et al. 1998), which inherently differ from deep-water processes due to the influence of a shallow ocean bottom and coastal wall, and have been observed to produce SST cooling in TCs up to 11°C (Glenn et al. 2016).

This paper analyzes a recent landfalling storm, Hurricane Irene (2011), using a combination of unique datasets. Hurricane Irene is an ideal case study because in the days leading up to its landfall in New Jersey (NJ), its intensity was overpredicted by hurricane models (i.e., “guidance”) and in resultant National Hurricane Center (NHC) forecasts (Avila and Cangialosi 2012). The NHC final report on the storm stated that there was a “consistent high bias [in the forecasts] during the U.S. watch–warning period.” NHC attributes one factor in this weakening to an “incomplete eyewall replacement cycle” and a resulting broad and diffuse wind field that slowly decayed as the storm moved from the Bahamas to North Carolina (NC)—over a warm ocean and in relatively light wind shear. Irene made landfall in NC as a category-1 hurricane, two categories below expected strength.

One hypothesis as to why Irene unexpectedly weakened between the Bahamas and NC involves both aerosols and ocean cooling (Lynn et al. 2016; Khain et al. 2016). Irene crossed a wide band of Sahara dust just north of the West Indies, initially causing convection invigoration in the simulated eyewall and fostering the hurricane’s development (Lynn et al. 2016). However, as Irene approached the United States, continental aerosols intensified convection at the simulated storm’s periphery. This intensification of convection at the TC periphery can lead to increases in TC central pressure and weakening of wind speed near the eyewall (Lynn et al. 2016 and references within).

This paper’s focus is on Irene’s time after its NC landfall (Fig. 1) and after it had weakened in intensity due to continental aerosol interaction with convection at the hurricane’s periphery and the slight SST cooling in the South Atlantic Bight (SAB). The SST cooling over the Mid-Atlantic Bight (MAB) was at least 3–5 times greater than the SST cooling that occurred in the SAB (Figs. 2 and 3).

While energetic ocean mesoscale features can distort the structure of the TC cold wake (Walker et al. 2005; Jaimes and Shay 2010; Jaimes et al. 2011), during the direct forcing part of the storm, TC cooling in a deep ocean with no eddy features is frequently distributed

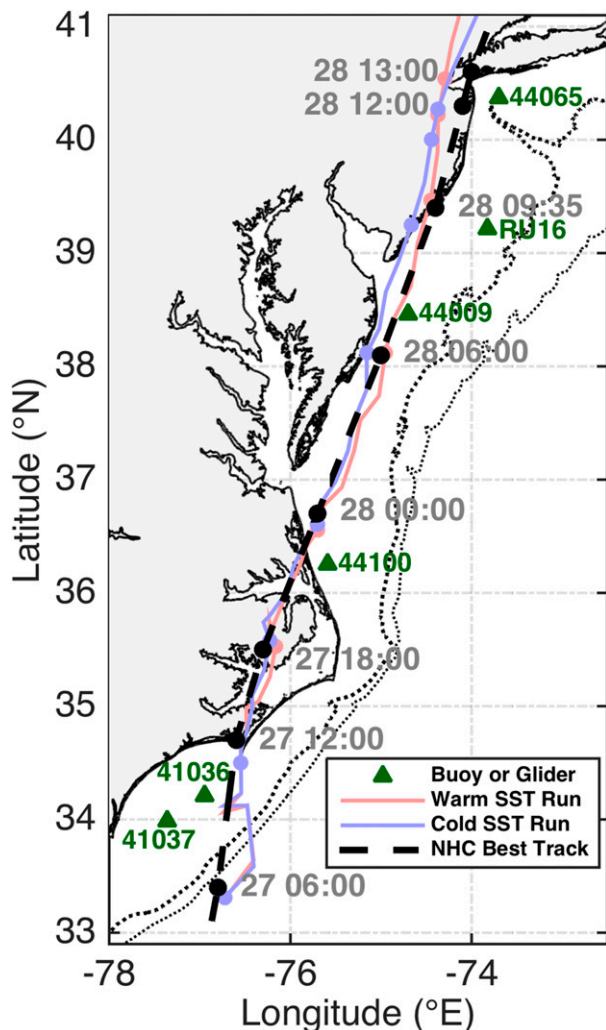


FIG. 1. NHC best-track data for Hurricane Irene in dashed black with timing (DD HH:MM August 2011) labeled in gray. Tracks for warm (red) and cold (blue) SST simulations are also plotted. NDBC buoy and glider RU16 locations are shown with green triangles. The 50- and 200-m isobaths are plotted in dotted black lines.

symmetrically between the front and back half of the storm (Price 1981). This does not include the inertial response in the cold wake. As will be shown in this paper, significant ahead-of-eye-center SST cooling (at least 6°C and up to 11°C, or 76%–98% of total in-storm cooling) was observed over the MAB continental shelf during Hurricane Irene, indicating that coastal baroclinic processes enhanced the percentage of cooling that occurred ahead of eye center (Glenn et al. 2016).

This paper will 1) explore how Irene’s predictions change using a semi-idealized treatment of the ahead-of-eye-center cooling, 2) show that better treatment would have lowered the high bias in real-time predictions, and 3) conclude that this ahead-of-eye-center cooling

observed in Irene was the missing contribution—not wind shear, track, or dry air intrusion—to the rapid decay of Irene’s intensity just prior to NJ landfall.

2. Data and methods

a. Gliders

Teledyne-Webb Research (TWR) Slocum gliders are autonomous underwater vehicles (AUVs) that have become useful platforms for monitoring the ocean’s response to storms (Glenn et al. 2008; Ruiz et al. 2012; Miles et al. 2013, 2015). Gliders can profile the water column from the surface to depths of up to 1000 m. They continuously sample every 2 s, providing a high temporal resolution time series from pre- to poststorm and complementing the spatial coverage that multiple concurrent airborne expendable bathythermograph (AXBT; Sessions et al. 1976; Sanabia et al. 2013) deployments can provide. Finally, gliders can be piloted, enabling more targeted profiling throughout the storm, in contrast to Argo (Gould et al. 2004; Roemmich et al. 2009) and Air-Launched Autonomous Micro-Observer (ALAMO; Sanabia and Jayne 2014; Sanabia et al. 2016) floats, which passively move with ocean currents. Because of this, gliders can be directed to steer into a storm and station-keep, providing a fixed-point Eulerian observation time series. A more detailed description of general capabilities of these gliders can be found in Schofield et al. (2007). For storm-specific capabilities of the gliders, see Miles et al. (2013, 2015) and Glenn et al. (2016).

Rutgers University Glider RU16 was used in this study. The glider was equipped with several science sensors, including a Seabird unpumped conductivity–temperature–depth (CTD) sensor, which measured temperature, salinity, and water depth. The top bin in the temperature profiles—0–1-m depth—is used to provide a measure of near-surface temperature at the glider location (Fig. 1). Thermal-lag-induced errors associated with the unpumped CTD were corrected before any data were used (Garau et al. 2011).

b. Buoys

1) NEAR-SURFACE TEMPERATURE

National Data Buoy Center (NDBC) buoys 41037 and 41036 in the SAB and buoys 44100, 44009, and 44065 in the MAB were used in this study (Fig. 1). Hourly water temperatures were used, which is measured at 0.6-m depth at all buoys except 0.46-m depth at 44100. These data provide near-surface water temperatures along and near the track of Hurricane Irene through the SAB and MAB.

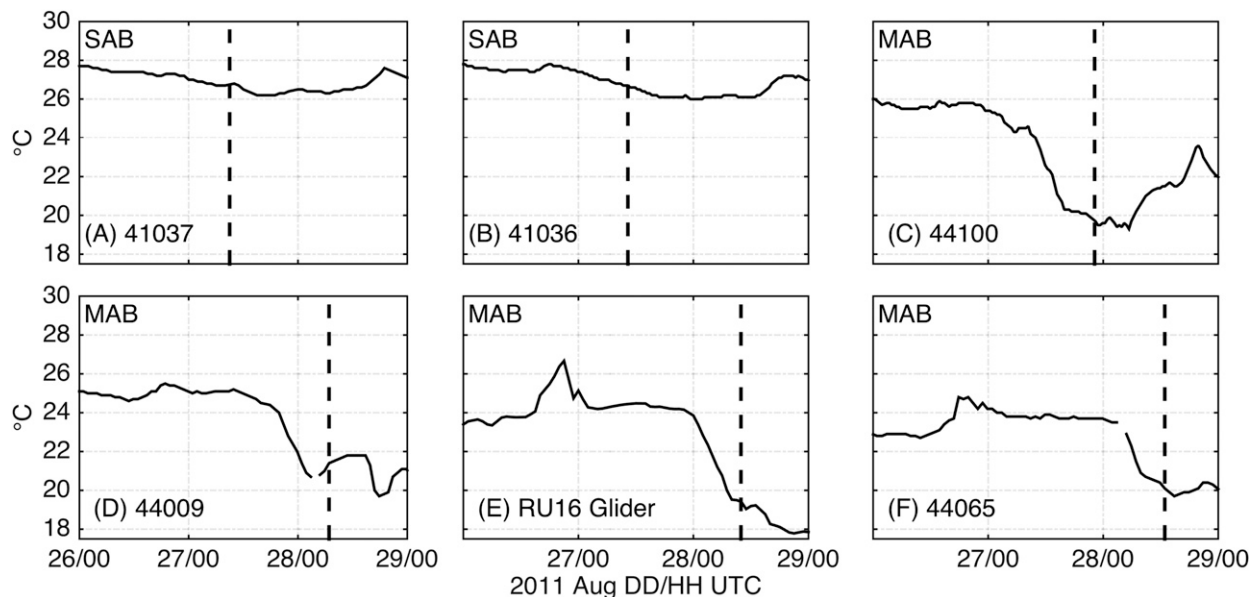


FIG. 2. NDBC buoy and glider near surface water temperature ($^{\circ}\text{C}$) time series. South Atlantic Bight buoys (denoted by “SAB”) from south to north are 41037 and 41036, and Mid-Atlantic Bight buoys and glider RU16 (denoted by “MAB”) from south to north are 44100, 44009, glider RU16, and 44065. Timing of Irene’s eye passage by the buoy or glider is denoted with vertical dashed line.

2) HEAT FLUXES

NDBC buoys 44009 and 44065 were used for latent and sensible heat flux calculations, which were estimated based on the “bulk formulas” (Fairall et al. 1996):

$$\text{Sensible heat flux: } H = -(\rho c_p) C_H U (\theta - \theta_{\text{sfc}}), \quad (1)$$

$$\text{Latent heat flux: } E = -(\rho L_v) C_Q U (q - q_{\text{sfc}}), \quad (2)$$

where ρ is density of air, c_p is specific heat capacity of air, C_H is sensible heat coefficient [see Eq. (5)], U is 5-m wind speed, θ is potential temperature of the air at 4 m and θ_{sfc} is potential temperature at the water surface, L_v is enthalpy of vaporization, C_Q is latent heat coefficient [see Eq. (6)], q is specific humidity of the air at 4 m, and q_{sfc} is interfacial specific humidity at the water surface.

Neither θ_{sfc} and q_{sfc} are directly computed from interfacial water temperature, but rather computed from buoy temperature measured at 0.6-m depth. During high wind conditions, the difference between skin temperature and temperature at 0.6-m depth is likely small enough to have a negligible effect on the computed bulk fluxes (Fairall et al. 1996).

c. Satellites

1) SEA SURFACE TEMPERATURE

The National Centers for Environmental Prediction (NCEP) Real-Time Global High-Resolution (RTG-HR) is a daily SST analysis used in this study. RTG-HR SST is

operationally produced using in situ and AVHRR data on a $1/12^{\circ}$ grid (Reynolds and Chelton 2010). The operational 13-km Rapid Refresh (RAP) and the 12-km North American Mesoscale Forecast System (NAM) and its inner nests, including the 4-km NAM continental U.S. (CONUS) nest, use fixed RTG-HR SST. Therefore, RTG-HR is the most relevant SST product for comparison with the 2-km SST composite described next.

Standard techniques to remove cloudy pixels in SST composites use a warmest pixel method because clouds are usually colder than the SST (Cornillon et al. 1987). This tends to reduce cloud contamination but results in a warm bias, which is unfavorable for capturing TC cooling. In this study, a 3-day “coldest dark-pixel” composite method is used to map regions of cooling from Irene. This technique, described in Glenn et al. (2016), filters out bright cloudy pixels while retaining darker ocean pixels.

2) WATER VAPOR

Satellites are also used for a spatial estimate of the intrusion of dry air into Irene’s circulation. *Geostationary Operational Environmental Satellite-13 (GOES-13)* water vapor channel-3 brightness temperature imagery is used for these estimates.

d. Radiosondes

Radiosondes, typically borne aloft by a weather balloon released at the ground, directly measure temperature, humidity, and pressure, and derive wind speed and direction. To validate profiles of modeled wind shear and

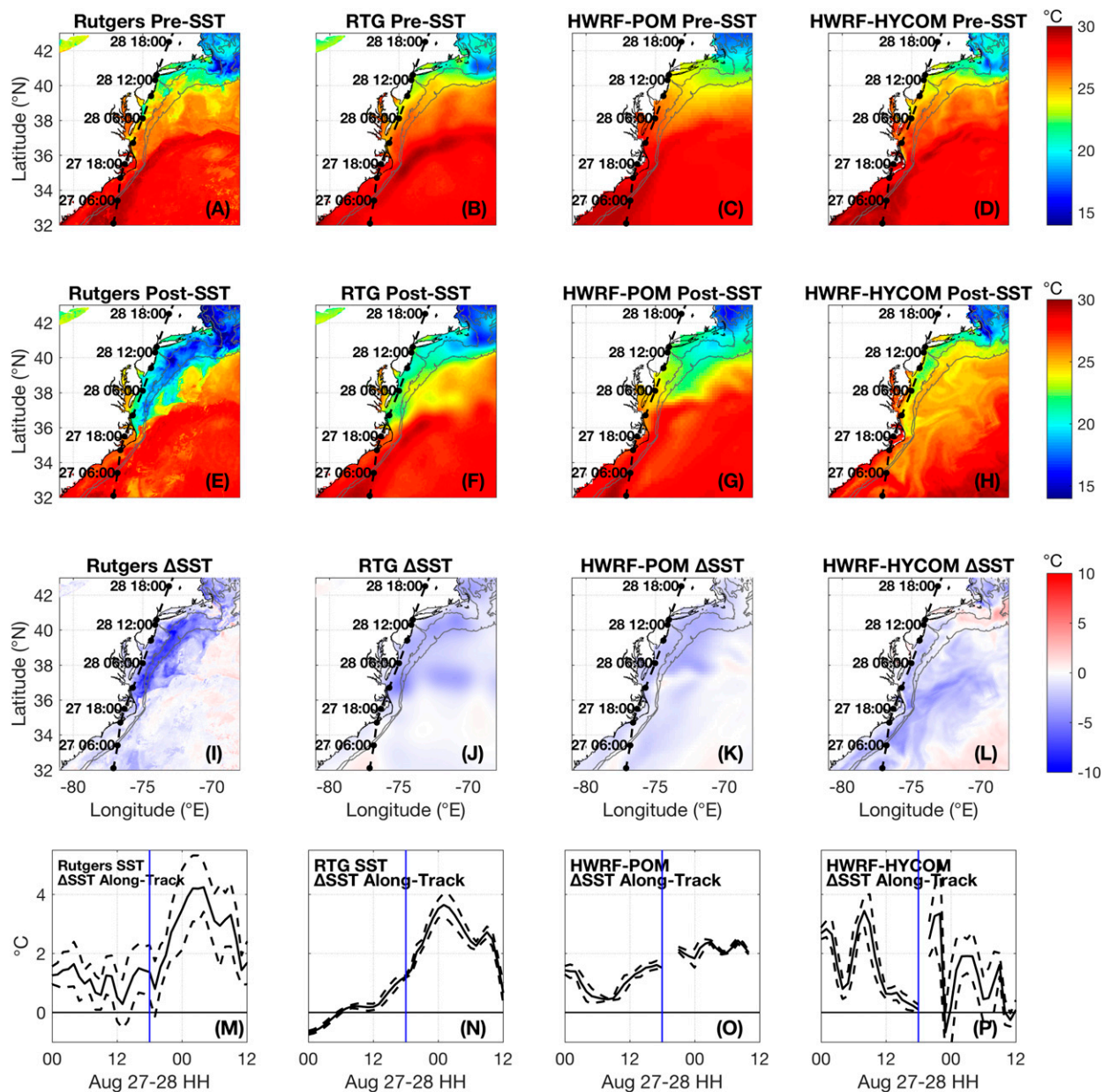


FIG. 3. SST plots (a)–(d) before Irene, (e)–(h) after Irene, (i)–(l) difference between before and after. (m)–(p) Along-track SST change (mean within 25 km of NHC best track in solid black, ± 1 standard deviation in dashed black) time series with vertical blue line dividing the first part of the time series when Irene was over the SAB, and the second part of the time series when Irene was over the MAB. (a), (e), (i), (m) The new Rutgers SST composite, as described in section 2c(1); before Irene is coldest dark-pixel composite from 24 to 26 Aug 2011, after Irene is from 29 to 31 Aug 2011. (b), (f), (j), (n) The Real-Time Global High Resolution (RTG HR) SST product from NOAA; before Irene is from 26 Aug, after Irene is from 31 Aug. (c), (g), (k), (o) The operational HWRP-POM from 2011, simulation initialized at 0000 UTC 26 Aug 2011; before Irene is from 0000 UTC 26 Aug, after Irene is from 0000 UTC 31 Aug. (d), (h), (l), (p) The experimental HWRP-HYCOM from 2011, simulation initialized at 0000 UTC 26 Aug 2011; before Irene is from 0000 UTC 26 Aug, after Irene is from 0000 UTC 31 Aug.

dry air intrusion, radiosonde observations of u and v winds are used from Albany, New York (KALB); Chatham, Massachusetts (KCHH); and Wallops Island, Virginia (KWAL), and RH is used from KALB and KWAL.

e. North American Regional Reanalysis

The North American Regional Reanalysis (NARR) is a 32-km, 45 vertical layer atmospheric reanalysis produced by NCEP and provides a long-term (1979–present)

set of consistent atmospheric data over North America (Mesinger et al. 2006). The data consist of reanalyses of the initial state of the atmosphere, which are produced by using a consistent data assimilation scheme to ingest a vast array of observational data into historical model hindcasts. NARR is used to evaluate modeled size and structure of Irene, modeled heat fluxes, and modeled wind shear, both horizontally and vertically.

f. Modeling and experimental design

1) HURRICANE WEATHER RESEARCH AND FORECASTING

Output from two different versions of the Hurricane Weather Research and Forecast system [HWRF; Skamarock et al. (2008)] was used in this study: 1) the 2011 operational HWRF, which was the Weather Research and Forecasting (WRF) Model coupled to the feature-model-based Princeton Ocean Model [HWRF-POM; Blumberg and Mellor (1987)], and 2) the same HWRF atmospheric component but coupled to the Hybrid Coordinate Ocean Model [HWRF-HYCOM; Chassignet et al. (2007)].

For the operational 2011 hurricane season, POM for HWRF-POM was run at $\frac{1}{6}^\circ$ resolution (~ 18 km), with 23 terrain-following sigma coordinate vertical levels. The three-dimensional POM output files contain data that are interpolated vertically onto the following vertical levels: 5-, 15-, 25-, 35-, 45-, 55-, 65-, 77.5-, 92.5-, 110-, 135-, 175-, 250-, 375-, 550-, 775-, 1100-, 1550-, 2100-, 2800-, 3700-, 4850-, and 5500-m depth (Tallapragada et al. 2011). Near-surface temperatures are pulled from the top level of POM, which occurs at 5 m.

The ocean model component of the 2011 HWRF-HYCOM system is the Real-Time Ocean Forecast System-HYCOM [RTOFS-HYCOM; Mehra and Rivin (2010)], which varies smoothly in horizontal resolution from ~ 9 km in the Gulf of Mexico to ~ 34 km in the eastern North Atlantic (Kim et al. 2014). Initial conditions are estimated from RTOFS-Atlantic (Mehra and Rivin 2010) 24-h nowcasts (Kim et al. 2014). RTOFS-HYCOM uses the Goddard Institute for Space Studies (GISS) vertical mixing and diffusion scheme (Canuto et al. 2001, 2002). Near-surface temperatures are pulled from the top layer of HYCOM, which ranges from less than 1 m in shallower regions (approximately 40-m water column depth or less) to 3 m in deeper regions (approximately 100-m water column depth or greater).

2) REGIONAL OCEAN MODELING SYSTEM

The Regional Ocean Modeling System [ROMS; <http://www.roms.org>; Haidvogel et al. (2008)] is a free-surface, sigma coordinate, primitive equation ocean model that

has been particularly used for coastal applications. Output is used from simulations run on the Experimental System for Predicting Shelf and Slope Optics (ESPreSSO) model (Wilkin and Hunter 2013) grid, which covers the MAB from Cape Hatteras to Cape Cod, from the coast to past the shelf break, at 5-km horizontal resolution and with 36 vertical levels.

3) WRF AND EXPERIMENTAL DESIGN

(i) Control simulation

The Advanced Research dynamical core of WRF [ARW, <http://www.wrf-model.org>, Skamarock et al. (2008)], version 3.4 is a fully compressible, nonhydrostatic, terrain-following vertical coordinate, primitive equation atmospheric model. This ARW domain extends from south Florida to Nova Scotia, and from Michigan to Bermuda (Glenn et al. 2016).

In the experiments, the control simulation has a horizontal resolution of 6 km with 35 vertical levels. The following physics options are used: longwave and shortwave radiation physics were both computed by the Rapid Radiative Transfer Model-Global (RRTMG) scheme, the Monin–Obukhov atmospheric layer model and the Noah land surface model were used with the Yonsei University planetary boundary layer (PBL) scheme, and the WRF double-moment 6-class moisture microphysics scheme (Lim and Hong 2010) was used for grid-scale precipitation processes. The control simulation did not include cumulus parameterization (Kain 2004); sensitivity to cumulus parameterization was tested in a subsequent simulation (see below and in Table 1).

It was critical to ensure that the control simulation had a track very similar to the NHC best track, so as to not include any additional land effects on Irene's intensity as it tracked closely along the coast. Also, because TC translation speed has a large impact on SST response and subsequent negative feedback on TC intensity (Mei et al. 2012), it was critical to closely simulate Irene's translation speed. Several different lateral boundary conditions and initialization times were experimented with before arriving at the best solution (after Zambon et al. 2014a). The resulting initial and lateral boundary conditions used are from the Global Forecast System (GFS) 0.5° operational cycle initialized at 0600 UTC 27 August 2011.

For the control simulation, RTG-HR SST from 0000 UTC 27 August 2011 is used for bottom boundary conditions over the ocean. This is 6 h prior to model initialization, to mimic NAM and RAP operational conditions. All simulations are initialized at 0600 UTC 27 August 2011 when Irene was just south of NC (Fig. 1) and end at 1800 UTC 28 August 2011. By initializing so late, the focus is only on changes in Irene's

TABLE 1. List of model sensitivities, grouped by type. Name of sensitivity is on left, details of sensitivity with WRF namelist option on right. Control run listed last.

Sensitivity	WRF namelist option
A. Model configuration	
1. Horizontal resolution (<i>dx</i>)	3 vs 6 km
2. Vertical resolution (<i>e_vert</i> , <i>eta_levels</i>)	51 vs 35 vertical levels
3. Adaptive time step (<i>use_adaptive_time_step</i>)	On vs off
4. Boundary conditions (update frequency, <i>interval_seconds</i>)	3 vs 6 h
5. Digital filter initialization (DFI, <i>dfi_opt</i>)	On (<i>dfi_nfilter</i> = 7) vs off
B. Atmospheric–model physics	
6–7. Microphysics (<i>mp_physics</i>)	6 (WRF single-moment 6-class) vs 16 (WRF double-moment 6-class) vs 30 (HUJI spectral bin microphysics, “fast”)
8–9. Planetary boundary layer scheme (<i>bl_pbl_physics</i>)	5 (Mellor–Yamada–Nakanishi–Niino level 2.5) vs 7 (ACM2) vs 1 (Yonsei University)
10. Cumulus parameterization (<i>cu_physics</i>)	1 (Kain–Fritsch, <i>cudt</i> = 0, <i>cugd_avedx</i> = 1) vs 0 (off)
11. SST skin (<i>sst_skin</i>)	On vs off
12–14. Longwave radiation (<i>ra_lw_physics</i>)	1 (RRTM) vs 5 (new Goddard) vs 99 (GFDL) vs 4 (RRTMG)
15–17. Shortwave radiation (<i>ra_sw_physics</i>)	1 (Dudhia) vs 5 (new Goddard) vs 99 (GFDL) vs 4 (RRTMG)
18–19. Latent heat flux < 0 over water (in <i>module_sf_sfclay</i>)	On vs off (warm SST) On vs off (cold SST)
20. Land surface physics (<i>sf_surface_physics</i>)	1 (5-layer thermal diffusion) vs 2 (Noah)
C. Advanced Hurricane WRF (AHW) options	
21–22. Air–sea flux parameterizations (<i>isftcflx</i>)	1 vs 0 (warm SST) (control run: <i>isftcflx</i> = 2) 1 vs 0 (cold SST) (control run: <i>isftcflx</i> = 2)
D. Sea surface temperature	
23–25. SST	Cold vs warm (<i>isftcflx</i> = 2) Cold vs warm (<i>isftcflx</i> = 1) Cold vs warm (<i>isftcflx</i> = 0)
E. Advanced Hurricane WRF (AHW) options (12-h later initialization)	
26. Digital filter initialization (DFI, <i>dfi_opt</i>)	On (<i>dfi_nfilter</i> = 7) vs off
27–28. 1D ocean mixed layer model (<i>sf_ocean_physics</i> = 1)	On (isothermal warm initial conditions) vs on (glider stratified initial conditions) vs off
29–30. 3D ocean Price–Weller–Pinkel model (<i>sf_ocean_physics</i> = 2)	On (HWRF-HYCOM initial conditions) vs on (glider stratified initial conditions) vs off

intensity occurring in the MAB. Further, as will be shown below, model spinup was a quick 6 h, so the model is already in a state of statistical equilibrium (Brown and Hakim 2013) under the applied dynamical forcing by the time Irene enters the MAB.

A two-part experiment, detailed below, is performed to investigate why model guidance did not fully capture the rapid decay of Irene just prior to NJ landfall. First, >140 simulations are conducted for sensitivities of Irene’s intensity, size, and structure to various model parameters, physics schemes, and options, including horizontal and vertical resolution, microphysics [including a simulation with WRF spectral bin microphysics (Khain et al. 2010) to test sensitivity to aerosols], PBL scheme, cumulus parameterization, longwave and shortwave radiation, land surface physics, air–sea flux parameterizations, coupling to a 1D ocean mixed layer (OML) model, coupling to a 3D ocean Price–Weller–Pinkel (PWP) model, and SST (Table 1). These simulations quantify and contextualize the sensitivities of Irene’s modeled intensity, size, and structure to SST. Second, a model assessment

is performed, specifically evaluating the control run’s treatment of track, wind shear, and dry air intrusion.

To conclude the data and methods section, details are provided on a few key sensitivities. These are the following: SST, air–sea flux parameterizations, 1D OML model, 3D PWP model, and latent heat flux < 0 over water.

(ii) Sensitivity to SST

To quantify the maximum impact of the ahead-of-eye-center SST cooling on storm intensity, the control run using a static warm prestorm SST (RTG-HR SST) is compared to a simulation using static observed cold poststorm SSTs. For this cold SST, the 29–31 August 2011 3-day coldest dark-pixel SST composite (described above) is used (Fig. 3e). According to underwater glider and NDBC buoy observations along Irene’s entire MAB track (Fig. 1), almost all of the SST cooling in the MAB occurred ahead of Irene’s eye center (Figs. 2c–f). The SAB also experienced ahead-of-eye-center SST cooling, but values are on the order of 1°C or less (Figs. 2a,b). Also, the model simulations include only 6 h of storm

presence over the SAB. Therefore, the SST simulations described above quantify the sensitivity of Irene to ahead-of-eye-center cooling that occurred only in the MAB.

(iii) *Sensitivity to air–sea flux parameterizations*

The bulk formulas for sensible and latent heat fluxes are listed above in the buoy heat flux description. The following is the equation for momentum flux:

$$\text{Momentum flux: } \tau = -\rho C_D U^2, \quad (3)$$

where ρ is density of air, C_D is drag coefficient, and U is 10-m wind speed.

Three options exist in ARW version 3.0 and later for air–sea flux parameterizations (WRF namelist option `isftcflx` = 0, 1, and 2). These parameterization options change the momentum (z_0), sensible heat (z_T), and latent heat (z_Q) roughness lengths in the following equations for drag, sensible heat, and latent heat coefficients:

$$\text{Drag coefficient: } C_D = \kappa^2 / [\ln(z_{\text{ref}}/z_0)]^2, \quad (4)$$

$$\text{Sensible heat coefficient: } C_H = (C_D^{1/2}) [\kappa / \ln(z_{\text{ref}}/z_T)], \quad (5)$$

$$\text{Latent heat coefficient: } C_Q = (C_D^{1/2}) [\kappa / \ln(z_{\text{ref}}/z_Q)], \quad (6)$$

where κ is the von Kármán constant and z_{ref} is a reference height (usually 10 m).

The reader is encouraged to refer to [Green and Zhang \(2013\)](#) for a detailed look at the impact of `isftcflx` = 0, 1, and 2 on roughness lengths, exchange coefficients, and exchange coefficient ratios C_H/C_D , C_Q/C_D , and C_K/C_D , where $C_K = C_H + C_Q$. Some key points from their paper are that, at wind speeds of 33 m s^{-1} or greater, `isftcflx` = 1 has the largest C_K/C_D ratio and shares with `isftcflx` = 2 the lowest C_D . As a result, they found that for Hurricane Katrina (2005), using `isftcflx` = 1 produced the most intense storm in terms of minimum SLP and maximum winds.

Therefore, our SST sensitivity effectively changes the variables θ_{sfc} and q_{sfc} in Eqs. (1)–(3) above, while our air–sea flux parameterization sensitivities change the equations for the momentum, sensible heat, and latent heat coefficients [Eqs. (4)–(6)] going into the respective flux Eqs. (1)–(3). Because `isftcflx` = 1 and `isftcflx` = 2 both include a term for dissipative heating and `isftcflx` = 0 does not in WRFv3.4 ([Green and Zhang 2013](#)), the air–sea flux parameterization sensitivity between `isftcflx` = 0 and 1, and between `isftcflx` = 0 and 2 also test the effect of turning on and off dissipative heating in the model. Although the dissipative heating term was removed as of WRFv3.7.1 due to controversy within the wind-wave

modeling community, dissipative heating is still considered an important issue in high wind regimes, and it has been shown to be capable of increasing TC intensity by 10%–20% as measured by maximum sustained surface wind speeds ([Liu et al. 2011](#)).

For the air–sea flux parameterization sensitivities, simulations are conducted with `isftcflx` = 0, 1, and 2 using both the warm (control) and cold SST boundary conditions.

(iv) *Sensitivities coupling WRF to 1D and 3D ocean models*

[Pollard et al.’s \[1972; described in WRF context by \[Davis et al. \\(2008\\)\]\(#\)\]](#) 1D ocean mixed layer model was used to test the sensitivity of Irene to 1D ocean processes. Two different initializations of the 1D ocean model were initially performed: 1) *coastal stratification*: initializing the mixed layer depth (MLD) everywhere to 10 m and the slope of the thermocline everywhere to $1.6^\circ \text{C m}^{-1}$ according to glider RU16’s observations ([Glenn et al. 2016](#)), and 2) *HYCOM stratification*: initializing the MLD and top 200-m mean ocean temperature spatially using HYCOM. However, there were major issues using both of these options to accurately determine sensitivity to 1D ocean processes. The issue with the first option is its requirement that the initialization is nonvariant in space; the Gulf Stream, which is included in the model domain, is very warm and well mixed down to 100–200 m ([Fuglister and Worthington 1951](#)). Initializing the Gulf Stream MLD to 10 m would result in cold water only 10 m deep being quickly mixed to the surface. The issue with the second option of using HYCOM is that due to its poor initialization, the HYCOM simulation used here did not resolve the abundant bottom cold water over the MAB continental shelf that was observed by glider RU16 prior to Irene ([Glenn et al. 2016](#)) and that is typical of the summer MAB cold pool ([Houghton et al. 1982](#)).

The 3D ocean PWP model ([Price et al. 1986, 1994](#)) was used to test the sensitivity of Irene to 3D open-ocean, deep-water processes, including Ekman pumping–upwelling and mixing across the base of the mixed layer caused by shear instability. While the 3D PWP model contains 3D dynamics and is fully coupled to WRF, it does not have bathymetry or a coastline ([Lee and Chen 2014](#)); water depth is uniform across the model grid. Therefore, any 3D PWP model run will not simulate the coastal baroclinic processes that were observed in Irene over the MAB continental shelf due to the presence of the coastline ([Glenn et al. 2016](#)). In addition, like in the 1D ocean model, initialization must be nonvariant in x – y space.

To ameliorate the issue with mixing the Gulf Stream and still conduct sensitivities on nonstatic 1D and 3D ocean processes, an initialization time 12 h later—1800

UTC 27 August instead of 0600 UTC 27 August—was used for the WRF-1D OML and WRF-3D PWP simulations, because Irene by then was already north of the Gulf Stream and thus would not interact with it, and still south of the MAB (see Fig. 1). Four sensitivities with this initialization time were tested with various configurations of the 1D OML and 3D PWP models. First, the 1D OML model was initialized using the prestorm coldest dark-pixel composite for SST and with a MLD of 200 m, to simulate isothermal warm ocean conditions and the effect of air–sea heat fluxes. Second, the 1D OML model was initialized everywhere using RU16 observed stratification, as described above; this simulated the effect of 1D deep-water mixing processes (the 1D OML model does not have an ocean bottom). Third, the 3D PWP model was initialized everywhere using the same RU16 observed stratification that was used for the 1D OML model simulation but with 400-m full water column depth, to simulate the effect of 3D deep-water processes. Fourth, the 3D PWP model was initialized everywhere using HWRF-HYCOM stratification at the RU16 glider location at 0000 UTC 26 August and again with 400-m full water column depth, to test the sensitivity to a poor ocean initialization. These simulations are summarized in Table 1.

(v) *Sensitivity to latent heat flux < 0 over water*

In the WRF surface layer scheme code, a switch exists that disallows any latent heat flux $< 0 \text{ W m}^{-2}$. (There is also a switch that disallows any sensible heat flux less than -250 W m^{-2} .) WRF convention for negative heat flux is downward, or from atmosphere to land or water surface. This sensitivity involves removing the switch disallowing negative latent heat flux. This switch removal only results in changes in latent heat flux over water, because the subsequent WRF land surface scheme modifies fluxes and already allows for latent heat flux to be negative over land.

3. Results

Sensitivity tests

1) MOTIVATION

Hurricane Irene developed into a tropical storm just east of the Lesser Antilles on 20 August 2011, strengthening into a category-1 hurricane just after landfall in Puerto Rico 2 days later. Irene continued to move northwest over the Bahamas, intensifying into a category-3 hurricane on 23 August. Soon after, a partial eyewall replacement cycle occurred and Irene was never able to fully recover, eventually weakening into a category-1

hurricane on 27 August as it neared NC. Irene remained at hurricane strength over the MAB until it made landfall in NJ as a tropical storm at 0935 UTC 28 August. As stated above, the NHC final report on Irene (Avila and Cangialosi 2012) conveyed a “consistent high bias [in the forecasts] during the U.S. watch–warning period,” which consisted of the time period when Irene was traversing the SAB and MAB (Avila and Cangialosi 2012).

The coastal track of Irene (Fig. 1) over the relatively highly instrumented mid-Atlantic allowed for a comprehensive look into the details and timing of coastal ocean cooling. All in-water instruments employed here provide fixed point data within 70 km from Irene’s eye, including station-keeping RU16, providing an Eulerian look at the ahead-of-eye-center cooling occurring near the storm’s inner core. RU16 profiled the entire column of water over the MAB continental shelf, providing a view of the full evolution of the upper-ocean response. The rapid two-layer shear-induced coastal mixing process that led to ahead-of-eye-center cooling is described in detail in Glenn et al. (2016).

The buoys in the SAB (41037 and 41036) documented $\sim 1^\circ\text{C}$ SST cooling in the storm’s front half, with total SST cooling less than 2°C (Fig. 2). Eye passage at each buoy is indicated by a vertical dashed line and represents the minimum sea level pressure (SLP) observed. For RU16, minimum SLP taken from the nearby WeatherFlow Tuckerton coastal meteorological station was used to calculate eye passage time, and for 44100, linearly interpolated NHC best-track data was used for eye passage time. In contrast to the SAB, the MAB buoys (44100, 44009, and 44065) as well as RU16 observed $4^\circ\text{--}6^\circ\text{C}$ SST ahead-of-eye-center cooling, with only slight cooling after eye passage of less than 2°C (Fig. 2). Therefore, the buoys and glider provide detailed evidence that significant ahead-of-eye-center cooling—76%–98% of the total observed in-storm cooling (Glenn et al. 2016)—occurred in the MAB.

While the buoys provided information on the timing of SST cooling, the high-resolution coldest dark-pixel SST composite showed the spatial variability of the cooling, revealing that the cooling was not captured by basic satellite products and some models used to forecast hurricane intensity. The improved 3-day coldest dark-pixel SST composite showed prestorm (24–26 August 2011; Fig. 3a) and poststorm (29–31 August 2011; Fig. 3e) SST conditions along the U.S. East Coast. SST cooling to the right of the storm track in the SAB approached 2°C , and in the MAB approached 11°C at the mouth of the Hudson Canyon (Fig. 3i). Under the TC inner core, within 25 km of Irene’s track, SST cooling in the SAB ranged from 0.5° to 1.5°C , while in the MAB cooling ranged from $\sim 2^\circ$ to $\sim 4^\circ\text{C}$ (Fig. 3m). It is important

Pressure and Wind Sensitivities: 8/27 2300- 8/28 1800 UTC

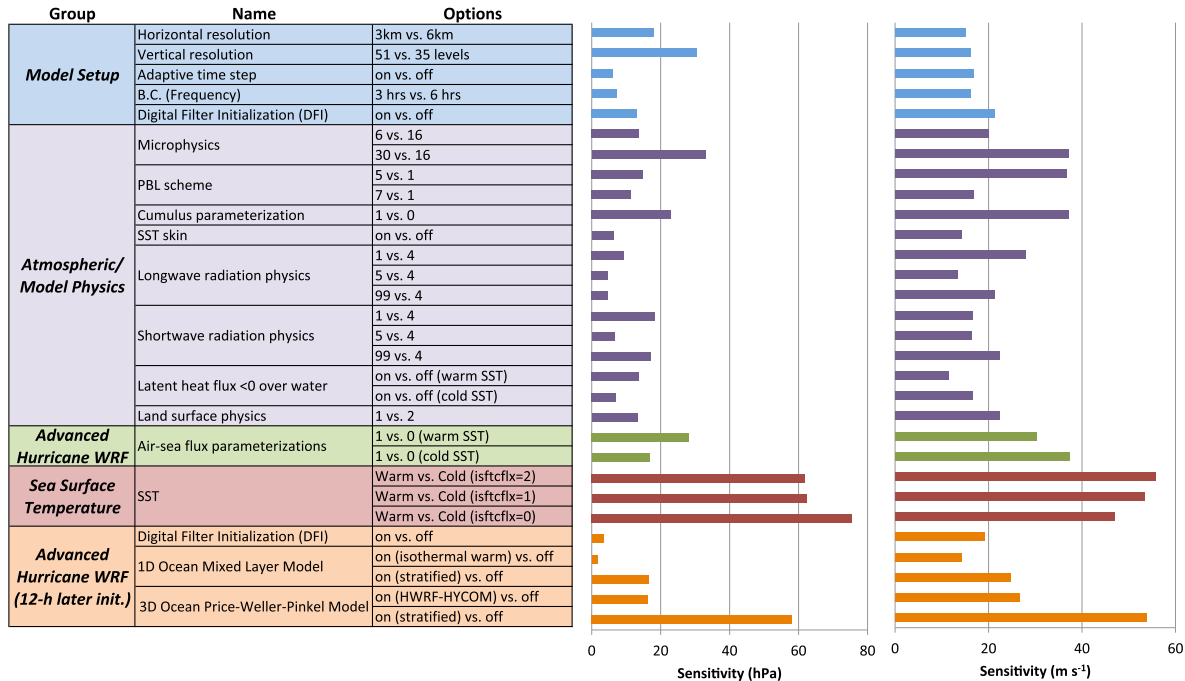


FIG. 4. Cumulative model sensitivity results from 2300 UTC 27 Aug 2011 (entrance of Irene's eye center over MAB) to 1800 UTC 28 Aug 2011 (end of simulation). (left) Group, name, and WRF namelist options with control run namelist option listed last for each sensitivity. (middle) Minimum sea level pressure (hPa) sensitivity and (right) maximum sustained 10-m wind (m s^{-1}) sensitivity.

to note that the SST composite from 3 days after storm passage was used for poststorm conditions. There were, indeed, large cloud-free areas over the MAB 1 day after storm passage, but it took an additional 2 days to fill in the remaining areas over the MAB and attain a cloud-free composite for input into WRF. In the persistently clear areas during this 3-day stretch, no additional SST cooling occurred during the poststorm inertial mixing period after the direct storm forcing.

RTG-HR SST pre- (26 August; Fig. 3b), poststorm (31 August; Fig. 3f), and difference (31 August minus 26 August; Fig. 3j) plots show spatially similar cooling patterns to the coldest dark-pixel SST composite, but cooling magnitudes are lower, especially to the right of the storm track in both the SAB and MAB (Fig. 3j). Similarly, there was no significant additional MAB cooling in RTG-HR SST from 1 day after (not shown) to 3 days after (Fig. 3f) storm passage.

HWRF-POM (Figs. 3c,g,k,o) and HWRF-HYCOM (Figs. 3d,h,l,p) model results are also shown as examples of coupled ocean-atmosphere hurricane models. Pre-storm (0000 UTC 26 August) and poststorm (0000 UTC 31 August) times for both model results are coincident with the coldest dark-pixel SST composite and RTG-HR SST composite times, and both model simulations shown are initialized at 0000 UTC 26 August. Therefore, the

poststorm SST conditions are 5-day forecasts in both models. Again, there are no significant differences in MAB SST cooling between immediately after and 3 days after Irene's passage in both HWRF-POM and HWRF-HYCOM. Like RTG-HR poststorm SST (Fig. 3f), HWRF-POM (Fig. 3g) and HWRF-HYCOM (Fig. 3h) poststorm SSTs in the MAB are several degrees too warm—the coldest SSTs are 20° – 23°C , where they should be 17° – 20°C . Therefore, these coupled atmosphere-ocean models designed to predict TCs did not fully capture the magnitude of SST cooling in the MAB that resulted from Hurricane Irene.

2) SENSITIVITY RESULTS

Over 140 WRF simulations were conducted to test the sensitivity of modeled Irene intensity to the observed ahead-of-eye-center cooling and to other model parameters. Only those simulations with tracks within 50 km of NHC best track were retained, leaving 30 simulations (Table 1).

To quantify cumulative model sensitivities, the sum of the absolute value of the hourly difference between the control run minimum SLP (and maximum sustained 10-m winds) and experimental run minimum SLP (and maximum 10-m winds) was taken, but only from 2300 UTC 27 August to the end of the simulation.

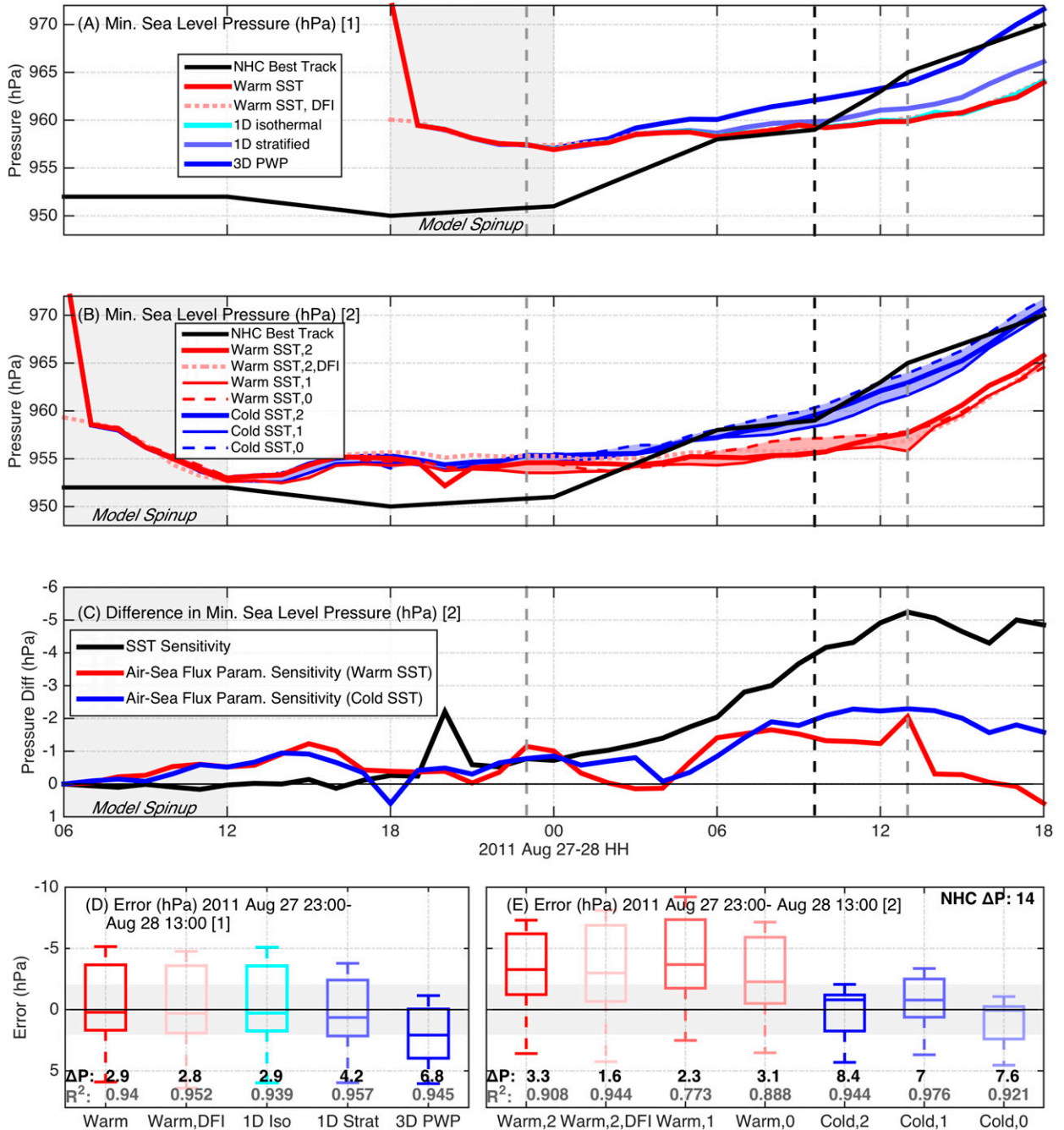


FIG. 5. Minimum SLP (hPa) time series for (a) WRF nonstatic ocean runs with NHC best track in black, warm SST in red, warm SST with DFI in dotted red, 1D ocean with isothermal warm initialization in cyan, 1D ocean with stratified initialization in light blue, and 3D PWP ocean in dark blue. (b) As in (a), but for WRF static ocean runs, with warm SST with isftcflx = 2 in red, warm SST with DFI in dotted red, warm SST with isftcflx = 1 in thin red, warm SST with isftcflx = 0 in dashed red, the three cold SST runs the same as warm SST but in blue lines. Vertical dashed gray lines depict start and end of Irene's presence over the MAB (2300 UTC 27 Aug–1300 UTC 28 Aug), with vertical dashed black line depicting Irene's landfall in NJ. Model spinup indicated as first 6 simulation hours with gray box. Difference in central pressure (c) between WRF static ocean warm and cold SST runs with isftcflx = 2 in black, between isftcflx = 0 and 1 for warm SST in red, and between isftcflx = 0 and 1 for cold SST in blue. (d) Box-and-whisker plots of errors vs NHC best-track data for WRF static ocean runs and (e) nonstatic ocean during Irene's MAB presence with R^2 values in gray and ΔP between 2300 UTC 27 Aug and 1300 UTC 28 Aug in black. NHC best-track ΔP in top right of (e), and uncertainty in pressure from NHC best-track data indicated by gray horizontal ribbon ± 0 in (d) and (e).

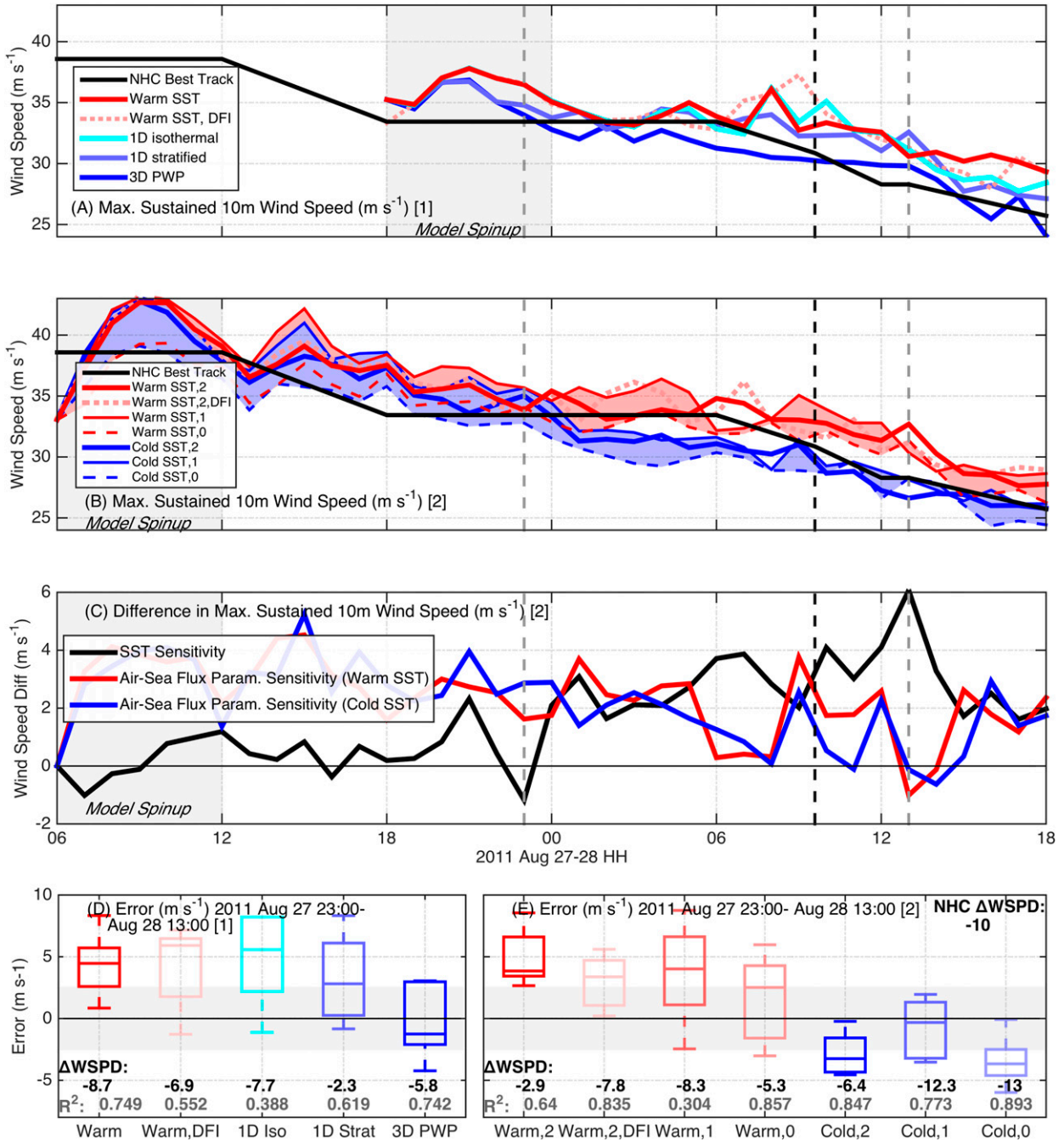


FIG. 6. As in Fig. 5, but for maximum sustained 10-m winds (m s⁻¹).

This confines the sensitivity to the time period of Irene’s presence over the MAB and thereafter. The equation is as follows:

$$\begin{aligned}
 & \sum_{i=1800\text{UTC}28\text{Aug}}^{i=2300\text{UTC}27\text{Aug}} |\text{min SLP}[\text{control}(\text{at hour } i)] \\
 & - \text{min SLP}[\text{exp}(\text{at hour } i)]|. \tag{7}
 \end{aligned}$$

Figure 4 shows the model sensitivities as measured by minimum SLP (left) and maximum 10-m wind speeds (right). Over the 19h calculated, the three largest sensitivities when considering both intensity metrics were due to SST with the three WRF air-sea flux parameterization options (isftcflx = 0, 1, 2). On average, for SST over the three options, pressure sensitivity was 66.6 hPa over the 19h (3.5 hPa h⁻¹) and wind sensitivity was 52.0 m s⁻¹ over

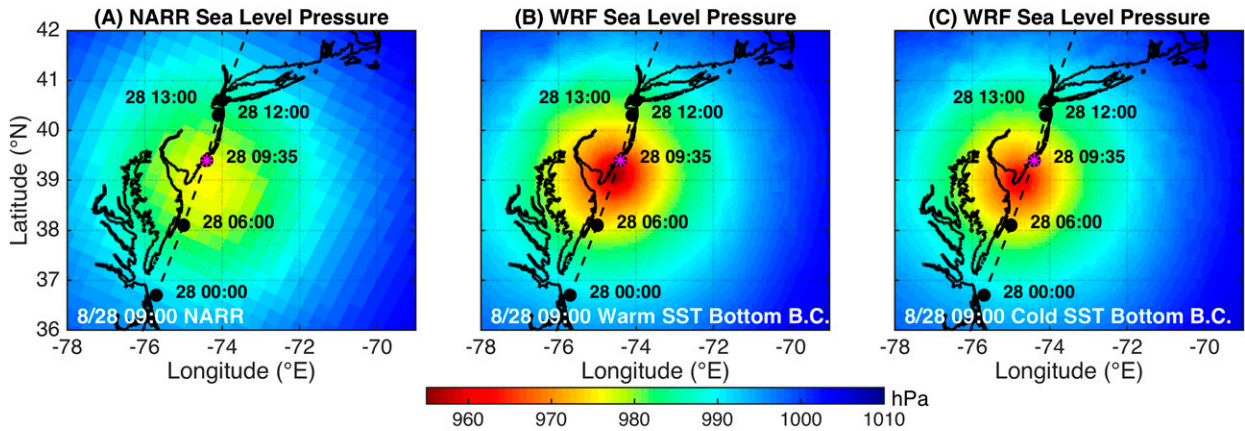


FIG. 7. Spatial plot of SLP (hPa) at 0900 UTC 28 Aug just prior to NJ landfall, with Irene’s NHC best track in dashed black: (a) NARR, (b) WRF with warm SST bottom boundary conditions, and (c) WRF with cold SST bottom boundary conditions.

the 19 h ($2.7 \text{ m s}^{-1} \text{ h}^{-1}$). Sensitivity to 3D open-ocean, deep-water processes through the use of the 3D PWP model was comparatively large (Fig. 4). However, caution must be taken with this simulation because the 3D PWP model does not have a coastline and bathymetry, and ended up producing more in storm SST cooling than was observed by glider RU16 (not shown).

The Advanced Hurricane WRF sensitivities for the 12-h later initialization (1D warm isothermal, 1D stratified, and 3D PWP) are presented in time series in Figs. 5a and 6a. The black line indicates NHC best-track estimates of intensity, while the red solid line indicates the fixed prestorm warm SST control run. Note that minimum SLP at initialization is about 973 hPa whereas NHC best track indicates 950 hPa at that time; this difference is due to issues with WRF’s vortex initialization (Zambon et al. 2014a), and it only takes 6 h for the model to adjust and drop 13 hPa to 959 hPa. The dotted red line indicates a sensitivity with digital filter initialization (DFI) turned on, which removes ambient noise at initialization. DFI resulted in initial min SLP (maximum winds) to be ~ 960 hPa (33 m s^{-1})—a reduction of 12 hPa (2 m s^{-1})—with downstream sensitivity negligible, demonstrating that the seemingly significant initialization issue likely has little significant effect on downstream intensity. The remaining sensitivities in Figs. 5a and 6a are the 1D ocean with isothermal warm initial conditions (effect of air–sea fluxes) in cyan, the 1D ocean with stratified initial conditions (effect of 1D mixing processes) in light blue, and the 3D PWP deep ocean with stratified initial conditions (effect of 3D deep-water processes) in dark blue. The air–sea fluxes have a negligible effect on intensity, while the 1D ocean mixing and 3D deep-water processes have a gradually larger negative effect on intensity.

The air–sea flux parameterization sensitivities with the standard initialization time are shown in Figs. 5b and 6b.

Again, the black line indicates NHC best-track estimates of intensity, and the simulations have issues with vortex initialization. The DFI sensitivity for this set of runs (dotted red) again effectively resolves this issue. The red lines indicate the three WRF air–sea flux parameterization options using the warm prestorm SST with the area between the $\text{isftcflx} = 0$ and 1 options shaded in red, and the blue lines and blue shading indicate the same but for the cold poststorm SST. Consistent with the results found by Green and Zhang (2013), $\text{isftcflx} = 1$ produced the most intense storm using both minimum SLP and maximum winds intensity metrics, for both the warm prestorm SST and cold poststorm SST; again, $\text{isftcflx} = 1$ has the largest C_K/C_D ratio and shares with $\text{isftcflx} = 2$ the lowest C_D .

Figures 5c and 6c show the time evolution of three sensitivities: 1) SST, warm versus cold (black), 2) air–sea flux parameterization with warm SST, $\text{isftcflx} = 0$ versus 1 (red), and 3) air–sea flux parameterization with cold SST, $\text{isftcflx} = 0$ versus 1 (blue). For both intensity metrics, sensitivity to SST gradually increases from about equal to flux parameterization sensitivity upon entrance to the MAB (first gray vertical dashed line) to almost triple it (~ 5 hPa vs ~ 2 hPa, 6 m s^{-1} vs $\sim 0\text{--}2 \text{ m s}^{-1}$) upon exit out of the MAB (second gray vertical dashed line). Finally, Figs. 5d,e and 6d,e show box-and-whisker plots of simulation error as compared to NHC best track, only during MAB presence (2300 UTC 27 August–1300 UTC 28 August), with uncertainty in NHC best-track data (Torn and Snyder 2012; Landsea and Franklin 2013) shown with gray shading. Correlation coefficient (R^2) values are shown at the bottom in gray, and ΔP and ΔWSPD are shown in black, with NHC ΔP and ΔWSPD values shown in the top right of Figs. 5e and 6e. These delta values, a measure of weakening rate, are calculated by taking the difference in

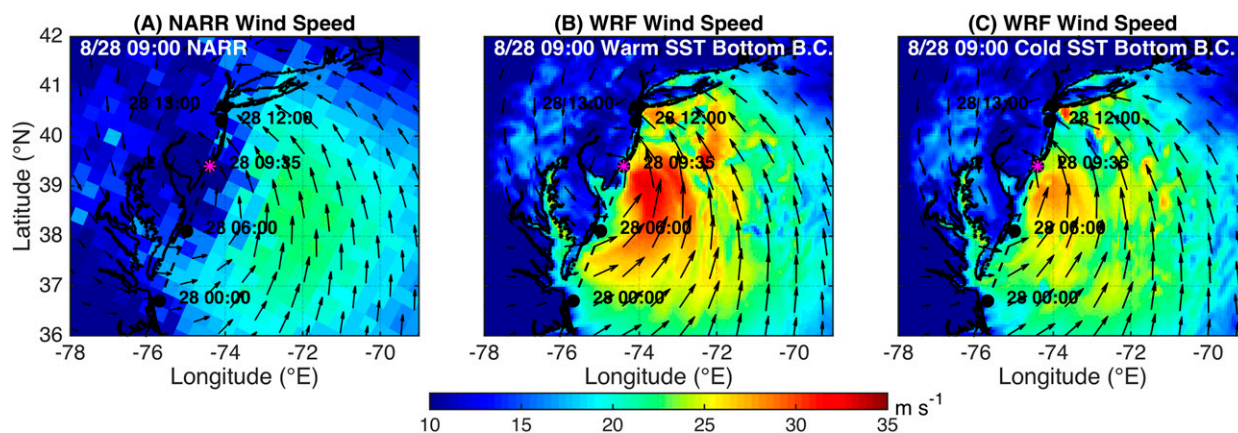


FIG. 8. As in Fig. 7, but for 10-m wind speeds and vectors (m s^{-1}).

pressure and wind speed between exit out of, and entrance into, the MAB.

Although the errors in minimum SLP for the simulations in Fig. 5d are low and the R^2 values are high, the errors in maximum winds are higher and the R^2 values are much lower in Fig. 6d. The four warm SST simulations (Figs. 5e and 6e) have a minimum SLP too low and maximum wind speed too high, while the three cold SST simulations have a minimum SLP closer to NHC best track and a maximum wind speed slightly lower than NHC best track. Because of the high uncertainty ($4\text{--}5 \text{ m s}^{-1}$ for nonmajor hurricanes) associated with NHC best-track wind estimates (Torn and Snyder 2012; Landsea and Franklin 2013), errors from the pressure metric are used. Minimum SLP is also a more certain measure of intensity because it is always at the TC eye center. The highest R^2 values and the ΔP values closest to NHC best-track ΔP were found with the three cold SST simulations. This indicates that a more accurate representation of the ahead-of-eye-center cooling via fixed cold poststorm SSTs lowers the high bias in our model's prediction of intensity. Further, the low ΔP -weakening rate attained using the 3D deep-water PWP simulation (ΔP : 6.8 hPa ; rate: 0.5 hPa h^{-1})—which again did not have a coastline or appropriately shallow ocean bottom—suggests that coastal baroclinic processes were responsible for the cooling that contributed to Irene's observed larger ΔP -weakening rate (ΔP : 14 hPa ; rate: 1 hPa h^{-1}). These coastal baroclinic processes, which are investigated in detail in Glenn et al. (2016), can be summarized as follows:

- (i) front half of Irene's winds were onshore toward the mid-Atlantic coastline;
- (ii) ocean currents in the surface layer above the sharp, shallow thermocline were aligned with the winds and also directed onshore over the MAB continental shelf;

- (iii) water piled up along the mid-Atlantic coast, setting up a pressure gradient force directed offshore;
- (iv) responding to the coastal piling of water, currents in the bottom layer below the sharp, shallow thermocline were directed offshore; and
- (v) opposing onshore surface layer and offshore bottom layer currents led to large shear across the thermocline and turbulent entrainment of abundant bottom cold water to the surface; this enhancement of shear and SST cooling occurred in the front half of Irene as long as the winds were directed onshore (hence the term "ahead-of-eye-center cooling").

Therefore, without the coastline in simulations, 1) the coastal piling of water, 2) the offshore bottom counterflow, 3) the enhanced shear at the thermocline, and 4) the rapid surface cooling would not be simulated.

Finally, the deep ocean simulations using the 1D ocean and the 3D ocean PWP model initialized with stratified conditions produced 32% and 56% of the in-storm ahead-of-eye-center cooling at the RU16 glider location, respectively (not shown). Meanwhile, 76% of the observed in-storm cooling at the RU16 glider location—and 82%, 90%, and 98% at 44009, 44065, and 44100,

TABLE 2. Radius of maximum 10-m winds (in km). Warm SST and cold SST simulations compared to b-deck data from the ATCF system database.

Time	Radius of max wind (km)		
	b-deck	Warm SST	Cold SST
0600 UTC 27 Aug	111	107	107
1200 UTC 27 Aug	83	80	80
1800 UTC 27 Aug	83	102	104
0000 UTC 28 Aug	83	72	85
0600 UTC 28 Aug	185	74	74
1200 UTC 28 Aug	185	213	280

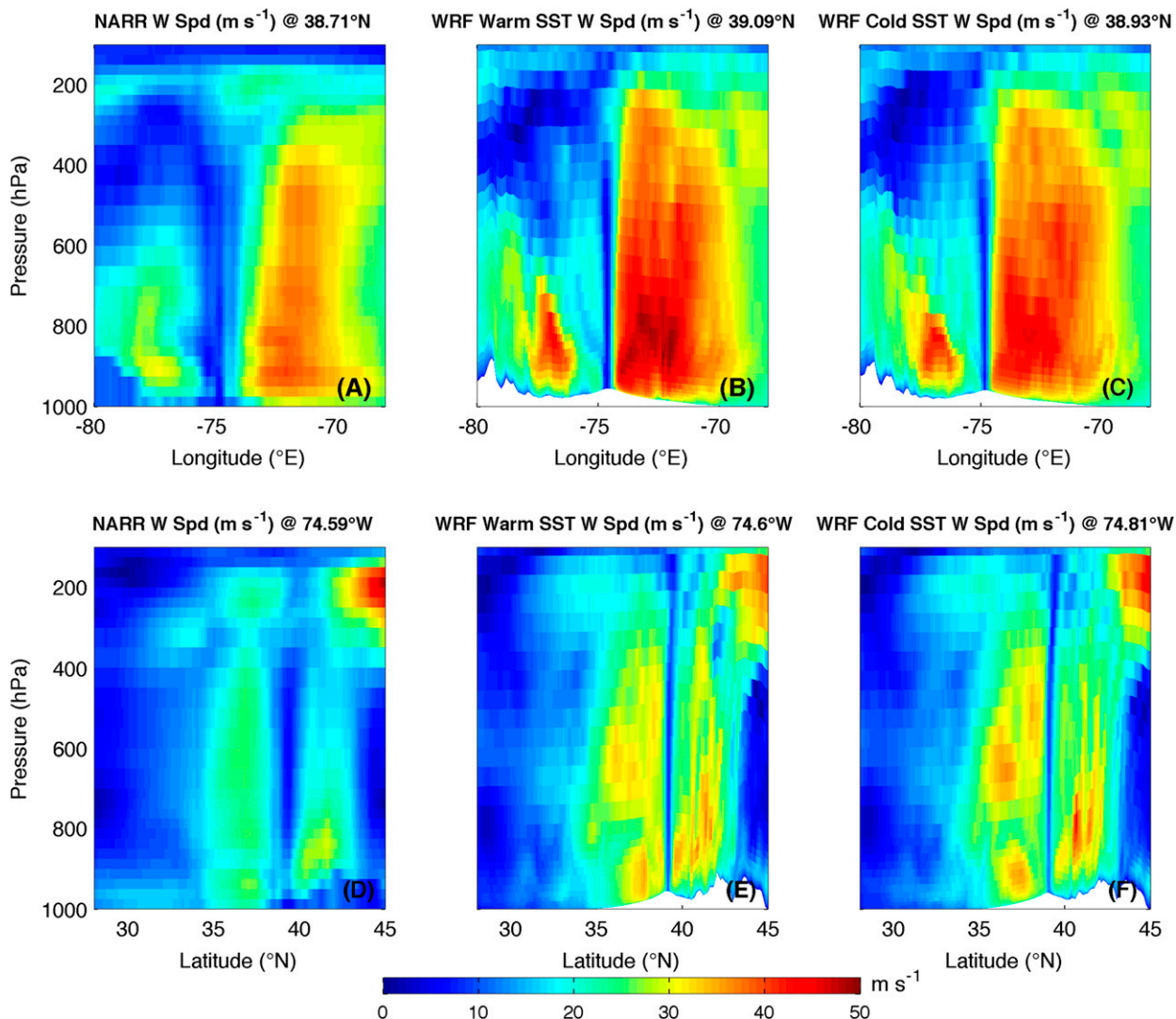


FIG. 9. Vertical cross sections of wind speed through Irene’s eye at 0900 UTC 28 Aug, just prior to NJ landfall. (a)–(c) west–east cross sections and (d)–(f) south–north cross sections. For each, the latitude and longitude of eye is determined by locating the minimum SLP for (a),(d) NARR; (b),(e) WRF with warm SST bottom boundary conditions; and (c),(f) WRF with cold SST bottom boundary conditions.

respectively—occurred ahead of the eye center (Fig. 2), further indicating that the nonsimulated coastal baroclinic processes enhanced the percentage of ahead-of-eye-center cooling in Irene.

How sensitive are Irene’s size and structure to SST? To spatially evaluate WRF results, NARR SLP and winds are used (Fig. 7). Spatial plots of SLP are shown from NARR (Fig. 7a), WRF warm SST (Fig. 7b), and WRF cold SST (Fig. 7c) runs, at just before NJ landfall. Only slight differences exist between WRF simulations, mainly in Irene’s central pressure (warm SST: 955.4 hPa, cold SST: 959.1 hPa); overall size and structure of the storm is very similar between runs. The WRF simulations also compare well in size and shape to NARR SLP, but do not in central pressure (NARR: 975.9 hPa). This

is likely due to lower NARR resolution, as the NHC best-track estimate of central pressure at landfall, only 35 min after, is 959 hPa. NARR, at 32-km resolution, is far too coarse to resolve inner-eyewall processes (Gentry and Lackmann 2010; Hill and Lackmann 2009).

Similar results are shown in spatial plots of 10-m winds (Fig. 8). General size and structure, especially over land, agree well among NARR, warm SST, and cold SST runs, but major differences exist over the MAB waters. NARR shows a maximum wind speed of 22.7 m s^{-1} , whereas the WRF warm SST (33.0 m s^{-1}) and cold SST (31.0 m s^{-1}) simulations are much closer to NHC best-track estimate of 30.9 m s^{-1} . Besides a general overall reduction in wind speed in the cold SST simulation, little difference is noted in size of Irene between warm and

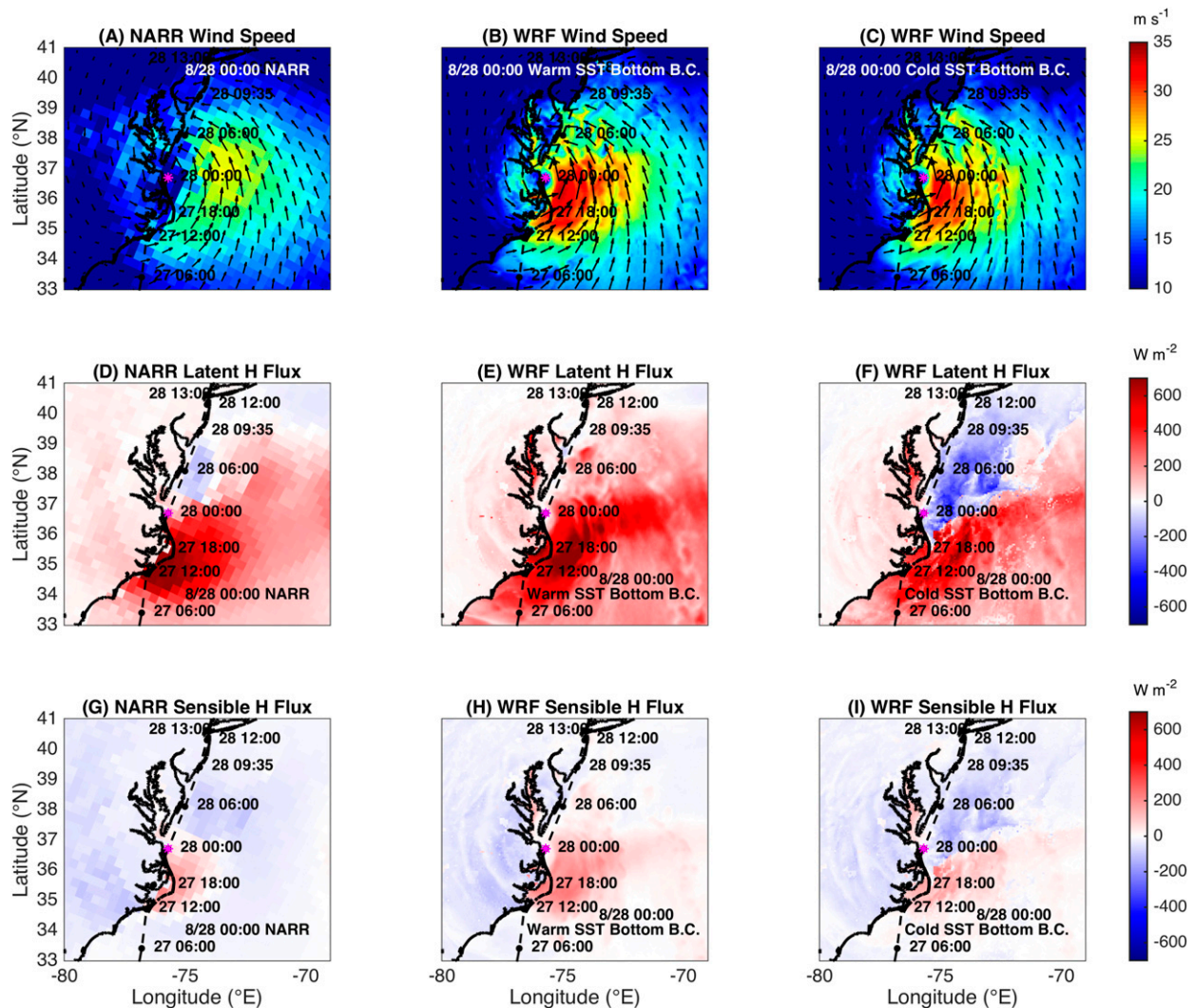


FIG. 10. (a)–(c) Spatial plots of 10-m wind speeds and vectors (m s^{-1}), (d)–(f) latent heat flux at the surface (W m^{-2}), and (g)–(i) sensible heat flux at the surface (W m^{-2}), at 0000 UTC 28 Aug. Fluxes are positive directed from water or land to atmosphere. (a), (d), (g) NARR is shown with fluxes shown as 3-h averages ending at 0000 UTC 28 Aug; (b), (e), (h) WRF is shown with warm SST bottom boundary conditions, with fluxes shown as instantaneous; and (c), (f), (i) WRF is shown with cold SST bottom boundary conditions (with negative latent heat flux allowed), with fluxes also shown as instantaneous.

cold SST. This is verified by a radius of maximum wind (RMW) comparison between the warm and cold SST simulations and b-deck data from the Automated Tropical Cyclone Forecast [ATCF; Sampson and Schrader (2000)] system database (Table 2). The data files within ATCF are within three decks known as a, b, and f decks. The b-deck data for Irene, available every 6 h, shows good agreement with both warm and cold SST simulations, with 13 km or less difference in RMW between warm and cold SST for the first 24 h of simulation, and 21 km or less difference in RMW between model and “observed” b-deck radii for the first 18 h of simulation. At 1200 UTC 28 August, the cold SST simulation shows a much larger RMW, likely due to the strongest winds

occurring in an outer band thunderstorm and indicating more rapid enlargement of storm size.

Vertical east–west (Figs. 9a–c) and north–south (Figs. 9d–f) cross sections of wind speeds through the eye of Irene at 0900 UTC 28 August, just before landfall, tell the same story—that NARR has issues reproducing the higher wind speeds not only at 10 m but through the entire atmosphere, and that there are only slight differences in wind speed structure between the warm and cold SST simulations. Both simulations show an asymmetric storm west–east with the core of the strongest winds over water, on the right side of the eye, extending all the way up to the tropopause at about 200 hPa (Figs. 9b and 9c), with the warm SST run showing much higher wind speeds

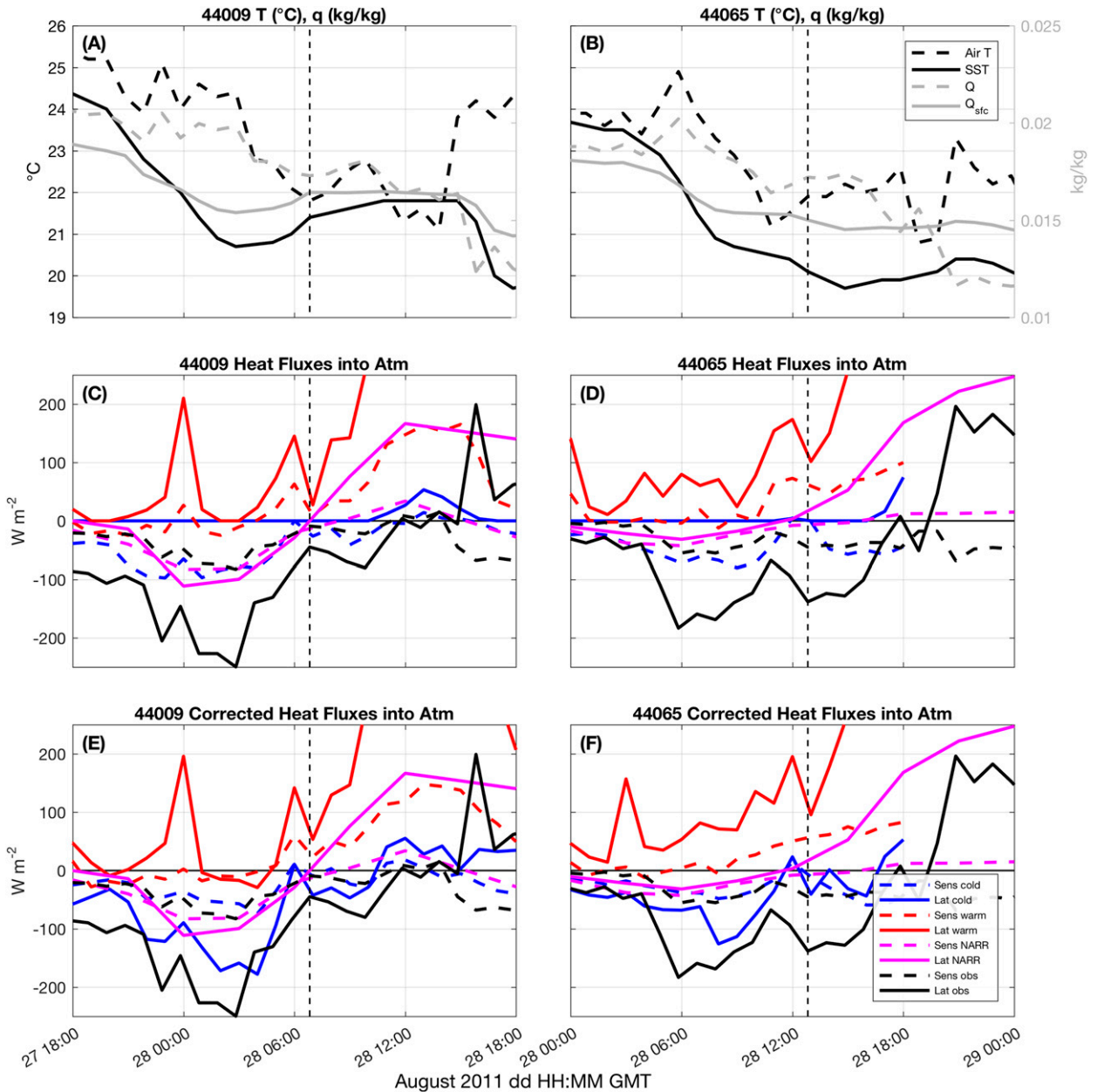


FIG. 11. Time series of air temperature (°C, black dashed), near-surface water temperature (°C, black solid), air specific humidity (kg kg^{-1} , gray dashed), and specific humidity at water surface (kg kg^{-1} , gray solid) at buoy (a) 44009 and (b) 44065, with vertical dashed line indicating timing of eye passage by that buoy (note the time axes are different for each buoy). (c) Sensible (dashed) and (d) latent (solid) heat fluxes (W m^{-2}) are shown for observed (black), NARR (magenta, 3-h flux averages), warm SST (red), and cold SST (blue). Fluxes are positive from ocean to atmosphere. (e),(f) The same fluxes are shown for observed and NARR as in (c),(d), but WRF fluxes are corrected to allow for negative latent heat flux over water.

from ~ 950 to 700 hPa. On the left side of the eye, the strongest winds extend only up to 700 – 800 hPa and the core is much narrower from west to east. The north–south cross sections show a more symmetric storm, as well as the outer edges of the jet stream at about 200 hPa and 45°N .

Because air–sea heat fluxes drive convection, TC circulation, and thus resulting TC intensity, a closer look at

the sensible and latent heat fluxes, specifically to determine just how sensitive they are to a change in SST, is warranted. The fluxes are plotted spatially at 0000 UTC 28 August in Fig. 10, and temporally at two MAB buoys in Fig. 11. The largest modeled latent and sensible heat fluxes correlate well spatially with the strongest winds in NARR, warm SST, and cold SST runs (Fig. 10).

However, there are large differences in both latent and sensible heat fluxes between the warm and cold SST runs, most notably over the MAB where a reverse in the sign of both latent and sensible heat flux occurs. In some locations over the MAB, the warm SST run shows a few hundred watts per meters squared in latent heat flux directed from the ocean to the atmosphere (Fig. 10e), whereas the cold SST run shows several hundred watts per meters squared in the opposite direction (Fig. 10f). NARR also shows slightly negative latent heat flux over the MAB (NARR fluxes are 3-h averages). Similar patterns are evident in sensible heat flux, but at a much smaller magnitude. It is again important to note that a negative latent heat flux over water—directed from the atmosphere to the ocean—is disallowed in WRF (similarly, sensible heat fluxes $< -250 \text{ W m}^{-2}$ are also disallowed over water). What is shown for the cold SST (warm SST) run in Fig. 10 is the cold SST (warm SST) simulation from sensitivity number 19 (18) (Table 1), with latent heat flux < 0 allowed over water. When negative latent heat flux is not allowed, all negative latent heat fluxes (e.g., the blue areas in Fig. 10f) become zero (not shown).

The negative latent heat fluxes were also “observed” at both buoys at which they were calculated—44009 and 44065. At both buoys, for almost the entire times shown, air temperature was greater than SST—in some cases over 4.5°C warmer—and air specific humidity was greater than specific humidity at water surface (Figs. 11a,b). The largest temperature and specific humidity differences occurred either during or right at the end of the SST cooling at each buoy, and coincided with the largest calculated observed negative sensible heat fluxes (-50 to -100 W m^{-2}) and negative latent heat fluxes (-200 to -250 W m^{-2}) at both buoys (Figs. 11c,d). These negative values are in stark contrast to the positive enthalpy fluxes (latent + sensible heat fluxes) of $O(1000) \text{ W m}^{-2}$ found under normal and rapid TC intensification scenarios (Lin et al. 2009; Jaimes and Shay 2015). At this time, NARR latent heat fluxes approached -120 W m^{-2} at 44009 and -40 W m^{-2} at 44065. The cold SST simulation shows latent heat fluxes zeroed out this whole time period (Figs. 11c,d), and approached -180 W m^{-2} at 44009 and -130 W m^{-2} at 44065 when negative latent heat fluxes are allowed (Figs. 11e,f). Meanwhile, the warm SST simulation shows latent heat fluxes with opposite sign, approaching 470 W m^{-2} toward the end of the simulation at 44009 and 530 W m^{-2} at 44065. Further, heat flux sensitivity to air–sea flux parameterizations was low, especially when compared to its sensitivity to warm versus cold SST. This evaluation of air–sea heat fluxes confirms that the cold SST simulation not only begins to resolve the negative latent heat fluxes that have been indicated

TABLE 3. Track error (in km) as compared to NHC best-track data, for the warm and cold SST simulations.

Time	Track error (km)	
	Warm SST	Cold SST
0600 UTC 27 Aug	12	12
1200 UTC 27 Aug	23	23
1800 UTC 27 Aug	13	11
0000 UTC 28 Aug	16	10
0600 UTC 28 Aug	5	14
0935 UTC 28 Aug ^a	8	28
1200 UTC 28 Aug	25	44
1300 UTC 28 Aug	26	48

^a Landfall in NJ.

by observations, but also approaches negative values that significantly affect storm intensity.

3) VALIDATION OF TRACK, WIND SHEAR, AND DRY AIR INTRUSION

To test our hypothesis that upper ocean thermal structure and evolution in the MAB was the missing contribution to Irene’s decay just before NJ landfall, the control run’s treatment of track, wind shear, and dry air intrusion was evaluated.

Track was handled very well by the simulations, remaining within 30 km for the entire time series for the control run and until landfall for the cold SST sensitivity (Fig. 1, Table 3). As Irene tracked so close to shore, this was critical for teasing out any potential impact from land interactions. In addition, control run translation speed over the MAB ($\sim 10 \text{ m s}^{-1}$) and cold SST sensitivity translation speed over the MAB ($\sim 10 \text{ m s}^{-1}$) were consistent with NHC best-track translation speed for Irene over the MAB ($\sim 10 \text{ m s}^{-1}$). For context, typical TC translation speed at 36° – 40°N (approximate MAB latitude range) is 8 – 10 m s^{-1} (Mei et al. 2012).

Wind shear values within and ahead of Irene during its MAB presence were similarly handled well by the simulations. At the time of entrance into the MAB, 200–850-hPa wind shear values in NARR, WRF warm SST, and WRF cold SST runs approached 60 m s^{-1} in the near vicinity ahead of Irene’s eye (Figs. 12a,c,e). Radiosonde launches from KALB, KCHH, and KWAL at the same time showed 200–850-hPa wind shear values of about 38, 34, and 15 m s^{-1} , respectively, which matched well with NARR (44, 29, and 22 m s^{-1}) and both WRF simulations (41, 33, and 17 m s^{-1} for warm SST; 39, 32, and 19 m s^{-1} for cold SST); furthermore, simulated u and v wind profiles across the entire atmospheric column correlated well with observed profiles (Figs. 12g,i,k). Twelve hours later, wind shear values ahead of Irene in NARR and both WRF simulations again approached 60 m s^{-1} , and observed wind shear at all three radiosonde sites

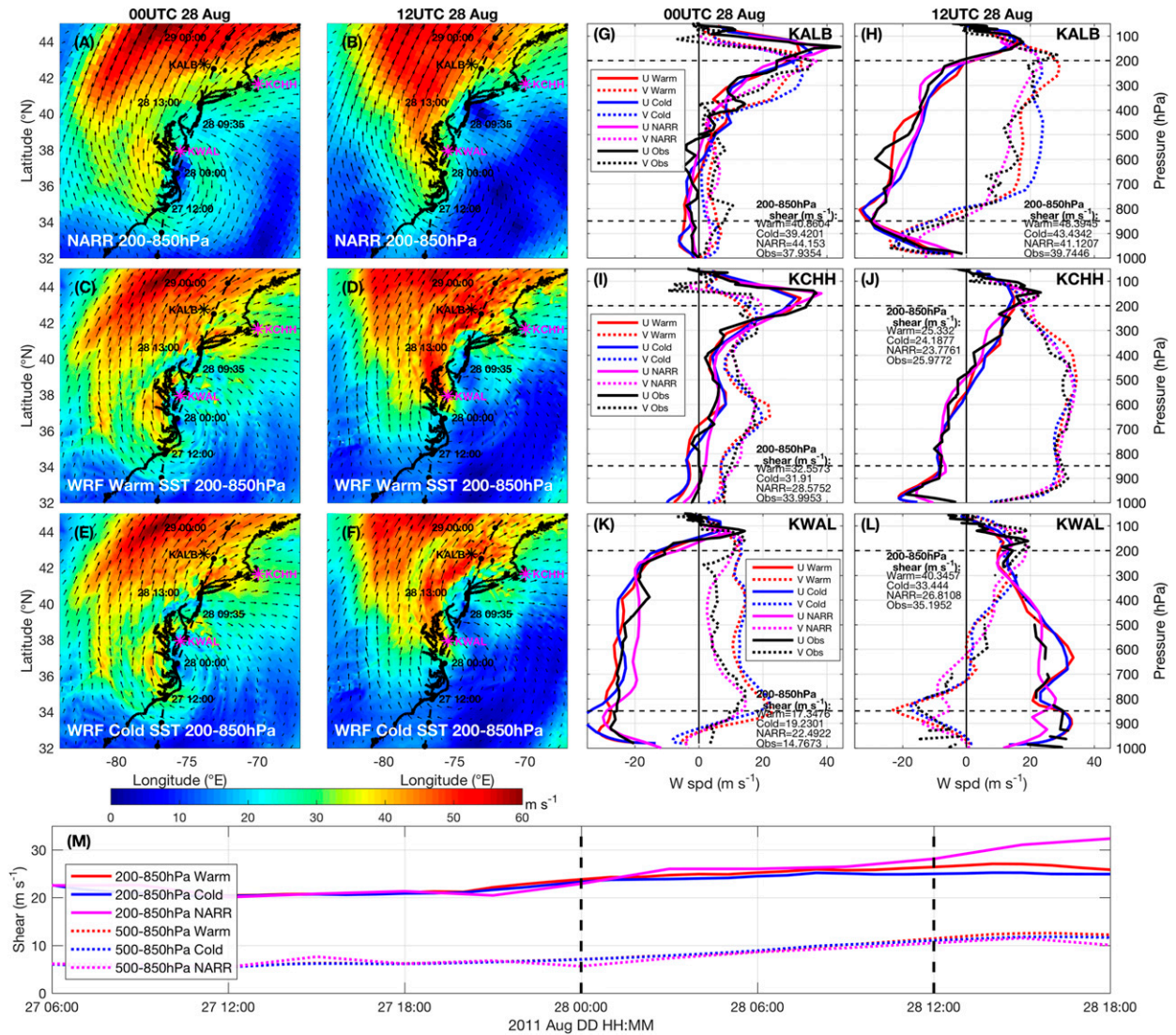


FIG. 12. Wind shear validation (a),(c),(e),(g),(i),(k) at 0000 UTC 28 Aug and (b),(d),(f),(h),(j),(l) at 1200 UTC 28 Aug. Spatial plots are the 200–850-hPa wind shear magnitude and vectors (m s^{-1}) with (a),(b) NARR; (c),(d) WRF warm SST; and (e),(f) WRF cold SST. KALB, KCHH, and KWAL indicated by labeled stars on maps and upper air radiosonde data at (g),(h) KALB; (i),(j) KCHH; and (k),(l) KWAL plotted, with solid lines for u winds (positive from west) and dashed lines for v winds (positive from south), and observed in black, NARR in magenta, WRF cold SST in blue, and WRF warm SST in red. The 200–850-hPa wind shear values (m s^{-1}) are labeled on graphs for observed, NARR, and WRF (cold and warm) simulations. (m) Time series of 200–850 hPa (solid) and 500–850 hPa (dotted) vertical shear (m s^{-1}) for WRF warm SST (red), WRF cold SST (blue), and NARR (magenta), with vertical dashed lines indicating times of (a)–(l).

correlated well with NARR and WRF (Figs. 12h,j,l). Finally, time series of 200–850- and 500–850-hPa wind shear values for NARR and WRF simulations were calculated by averaging wind shear values within an annulus 200–800 km from Irene’s center (Rhome et al. 2006; Zambon et al. 2014b). The 200–850-hPa wind shear values increase from approximately 20 m s^{-1} at 1200 UTC 27 August to $25\text{--}30 \text{ m s}^{-1}$ by the end of the simulation. These wind shear values were likely extremely detrimental to Irene’s intensity. Our WRF simulations accurately reproduced these very high

values and thus our model captured this important contribution to Irene’s decay.

Finally, a snapshot of RH at 200 and 700 hPa from WRF at 1200 UTC 28 August shows an intrusion of dryer air into the southeast quadrant of Irene, agreeing well with a GOES-13 water vapor image 12 min later (Figs. 13a–e). This GOES-13 image indicates dry upper levels (~ 200 hPa) and moist lower levels (~ 700 hPa) in the southern half of the storm. In the northern half of the storm there are moist upper and lower levels. Our WRF simulations match well in both halves. WRF simulations

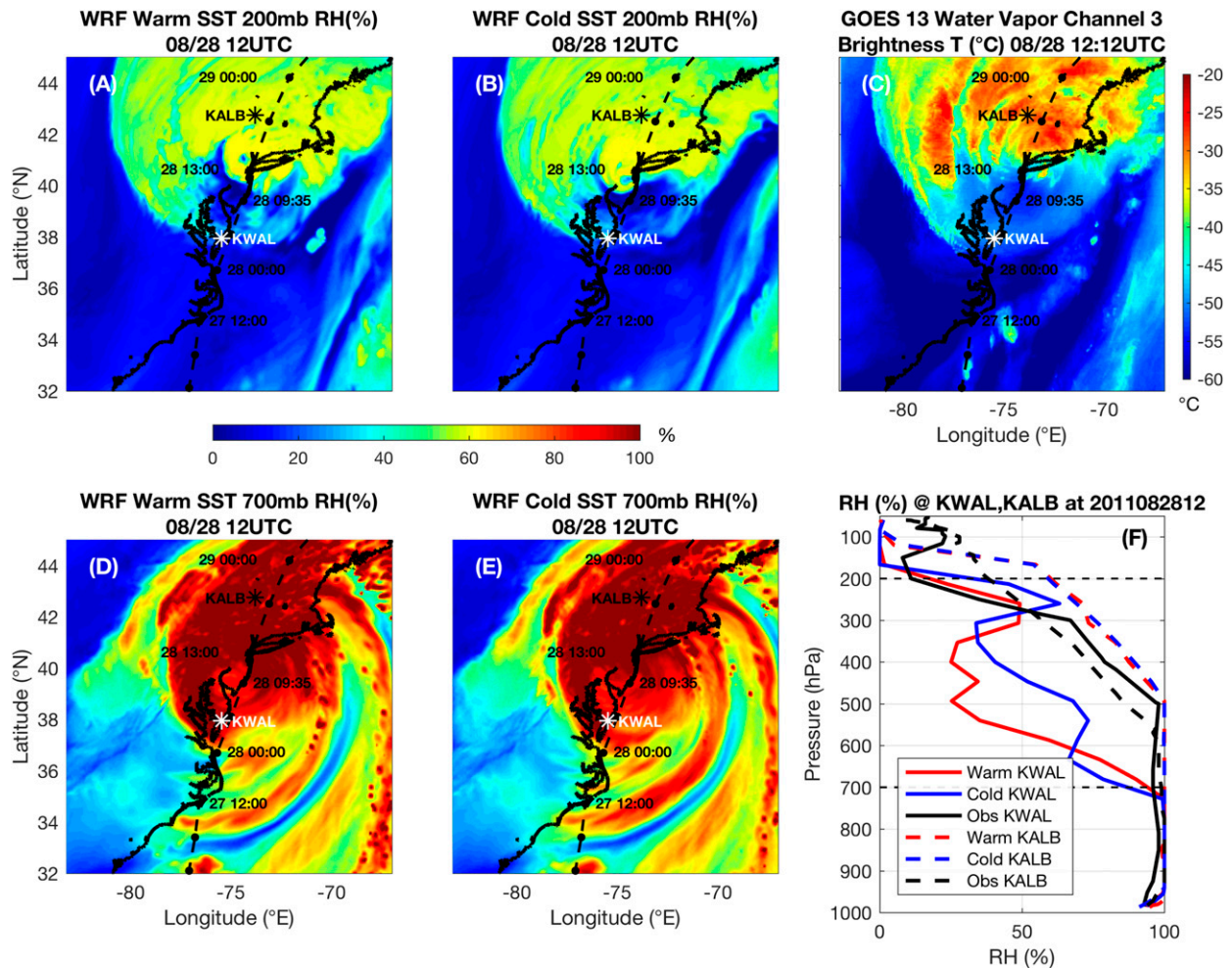


FIG. 13. Dry air intrusion validation (relative humidity, RH, %) at 1200 UTC 28 Aug with (a),(d) WRF warm SST; (b),(e) cold SST; and (c),(f) observations. (c) *GOES-13* water vapor channel-3 brightness temperature ($^{\circ}\text{C}$) at 1212 UTC 28 Aug and (f) upper air radiosonde relative humidity (%) at KWAL (KALB in dashed) with observed in black, WRF warm SST in red, and WRF cold SST in blue. (a), (b) WRF RH (%) at 200 mb for upper atmosphere, and (d),(e) WRF RH (%) at 700 mb for mid- to lower atmosphere. KWAL (KALB) location is shown in white (black), and the NHC best track is shown in black in spatial plots.

are also consistent with observations from a KALB radiosonde (Fig. 13f, dashed lines), which was in the storm's northern half at this time and showed moist lower levels and relatively moist upper levels. Comparisons with a KWAL radiosonde (Fig. 13f, solid lines), which was in the storm's southern half at this time, showed WRF actually drying out the atmosphere more than observed between approximately 700 and 300 hPa. Overdrying the mid-levels would result in additional decreases in storm intensity, so it is clear that dry air intrusion was also not a neglected contribution to Irene's decay.

4. Discussion

In summary, significant ahead-of-eye-center SST cooling (at least 6°C and up to 11°C , or 76%–98% of in-storm

cooling) was observed over the MAB continental shelf during Hurricane Irene. Standard coupled ocean–atmosphere hurricane models did not resolve this cooling in their predictions, and operational satellite SST products did not capture the result of the cooling. In this paper, the sensitivity of Irene's intensity, size, and structure to the ahead-of-eye-center SST cooling was quantified. The intensity sensitivity to the ahead-of-eye-center cooling turned out to be the largest among tested model parameters, surpassing sensitivity to the parameterization of air–sea fluxes themselves. Storm size and structure sensitivity to the ahead-of-eye cooling was comparatively low.

Furthermore, accounting for the ahead-of-eye-center SST cooling in our modeling through the use of a fixed cold poststorm SST that captured the cooling mitigated the high bias in model predictions. Validation of modeled

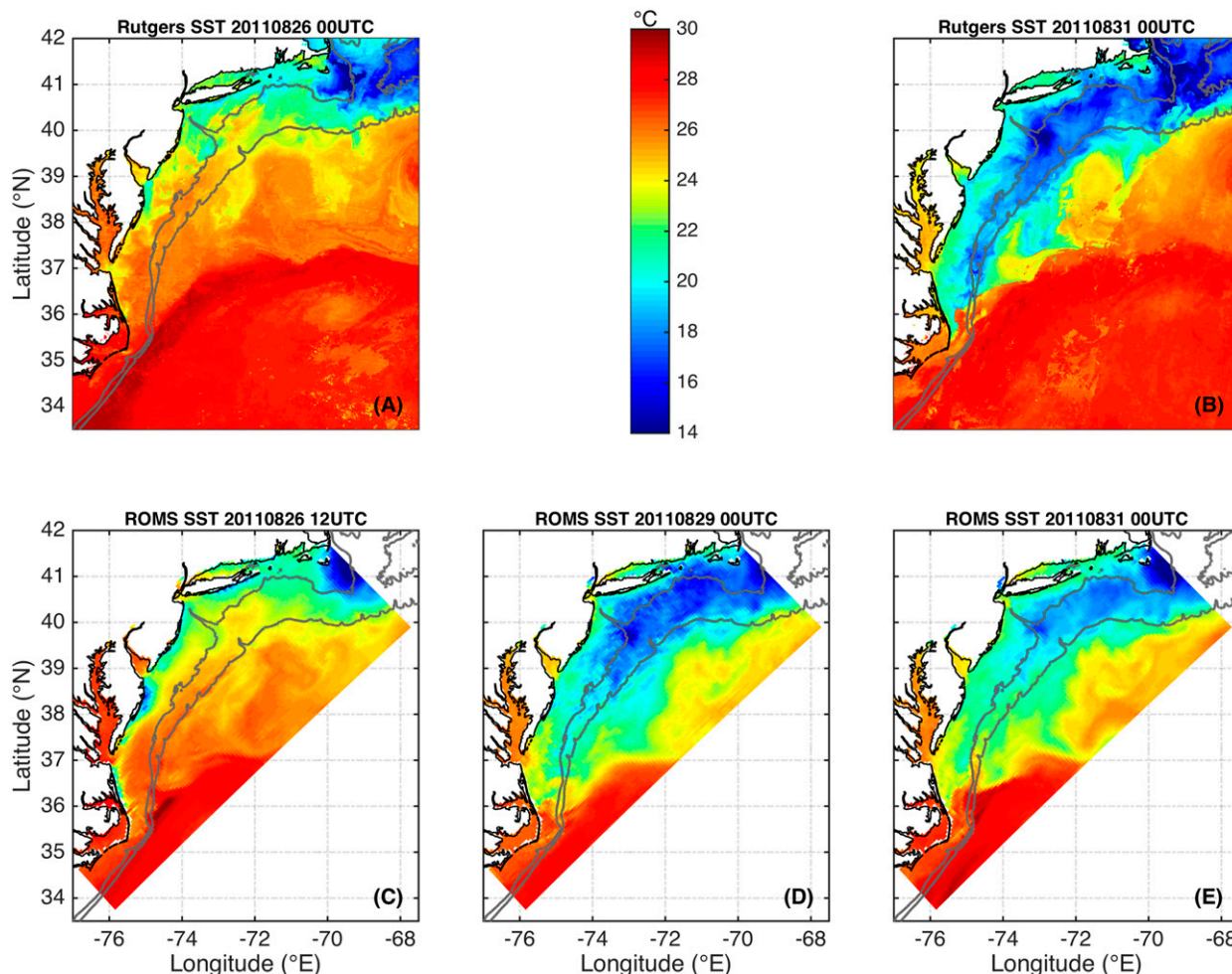


FIG. 14. SST from the new Rutgers SST composite in (a) from before Irene at 0000 UTC 26 Aug to (b) after Irene at 0000 UTC 31 Aug. The water temperature of top layer from a simulation using the ROMS ESPreSSO grid, (c) before Irene at 1200 UTC 26 Aug (simulation initialization), (d) just after Irene at 0000 UTC 29 Aug, and (e) well after Irene at 0000 UTC 31 Aug.

heat fluxes indicated that the cold SST simulation accurately reversed the sign of latent heat flux over the MAB as observed by two NDBC buoys. This would confirm the use of poststorm SST fixed through simulation so that Irene would propagate over the colder “premixed” waters, even though some slight cooling did indeed occur after eye passage. Finally, the simulations handled track, wind shear, and dry air intrusion well, indicating that upper ocean thermal evolution was the key missing contribution to Irene’s decay just prior to NJ landfall.

Simplistic 1D ocean models are incapable of resolving the 3D coastal baroclinic processes responsible for the ahead-of-eye-center cooling observed in Irene, consistent with Zambon et al. (2014a) in their study of Hurricane Ivan (2004). Rather, a 3D high-resolution coastal ocean model, such as ROMS, nested within a synoptic- or global-scale ocean model like HYCOM and initialized with realistic coastal ocean stratification, could

begin to spatially and temporally resolve this evidently important coastal baroclinic process (as described above in the “results” section), adding significant value to TC prediction in the coastal ocean—the last hours before landfall where impacts (storm surge, wind damage, and inland flooding) are greatest and are most closely linked with changes in storm intensity.

A ROMS simulation at 5-km horizontal resolution over the MAB not specifically designed for TCs can begin to resolve this ahead-of-eye-center cooling spatially (Fig. 14). This moderately accurate treatment of TC cooling, however, was arrived at through the combination of weak wind forcing from NAM (maximum winds $\sim 10 \text{ m s}^{-1}$ too low) and a broad initial thermocline, thus providing a right answer for the wrong reasons. Some issues with SST cooling from ROMS remain, including insufficient cooling in the southern MAB and surface waters warming too quickly poststorm. Further improvements may be realized with:

- 1) Better initialization to resolve and maintain the sharp initial thermocline and abundant bottom cold water.
- 2) Better mixing physics/turbulence closure schemes to accurately widen and deepen the thermocline upon storm forcing.
- 3) More accurate wind forcing and air–sea flux coefficients.

These suggestions are consistent with the recommendations of Halliwell et al. (2011), who studied Hurricane Ivan (2004) in detail as it moved over the relatively deeper and less stratified waters of the Gulf of Mexico. Future research will be conducted to test these ocean model improvements.

Other future work is threefold. First, better ocean data (e.g., more coastal ocean profile time series from flexible platforms like underwater gliders), will be needed to better spatially validate ocean models and identify critical coastal baroclinic processes. Second, Glenn et al. (2016) identified 10 additional MAB hurricanes since 1985, as well as Super Typhoon Muifa (2011) over the Yellow Sea, that exhibited ahead-of-eye-center cooling in stratified coastal seas. In-depth investigation of these storms, the response of the coastal baroclinic ocean, and the feedbacks to storm intensities will be crucial. Finally, movement toward a fully coupled modeling system is critical. Studies like this help isolate specific processes that components of coupled models should simulate.

Acknowledgments. Support was provided by New Jersey Board of Public Utilities (2010RU-COOL, BP-070), the Environmental Protection Agency (EP-11-C-000085), New Jersey Department of Environmental Protection (WM13-019-2013), National Oceanic and Atmospheric Administration (NOAA) led Integrated Ocean Observing System through the Mid-Atlantic Regional Association Coastal Ocean Observing System (MARACOOS, NA11NOS0120038), NOAA Cooperative Institute for the North Atlantic Region (NA13OAR4830233, Disaster Recovery Act), Teledyne Webb Research, and Rutgers University. We thank Hyun-Sook Kim and Zhan Zhang of the HWRF team at NCEP for providing the HWRF-POM and HWRF-HYCOM data. We also thank John Wilkin at Rutgers University for his suggestions regarding the ocean modeling and upper-air validation, the Rutgers Ocean Modeling research associates for their ROMS help, and the RU COOL group for their support and ideas. We thank Louis Bowers for his help with WRF, Hugh Roarty for his ocean observational guidance, and Rich Dunk for his helpful meteorological discussions and ideas. Finally, we thank David Titley, Jim Price, Joe Zambon, and the anonymous reviewers for their useful comments.

REFERENCES

- Avila, L. A., and J. Cangialosi, 2012: Tropical Cyclone Report: Hurricane Irene. National Hurricane Center Tropical Cyclone Rep. AL092011, 45 pp. [Available online at http://www.nhc.noaa.gov/data/tcr/AL092011_Irene.pdf.]
- Bender, M. A., I. Ginis, and Y. Kurihara, 1993: Numerical simulations of tropical cyclone-ocean interaction with a high-resolution coupled model. *J. Geophys. Res.*, **98**, 23 245–23 263, doi:10.1029/93JD02370.
- Blumberg, A. F., and G. L. Mellor, 1987: A description of a three-dimensional coastal ocean circulation model. *Three-Dimensional Coastal Ocean Models*, N.S. Heaps, Ed., Amer. Geophys. Union, 1–16.
- Brooks, D. A., 1983: The wake of Hurricane Allen in the western Gulf of Mexico. *J. Phys. Oceanogr.*, **13**, 117–129, doi:10.1175/1520-0485(1983)013<0117:TWOHAI>2.0.CO;2.
- Brown, B. R., and G. J. Hakim, 2013: Variability and predictability of a three-dimensional hurricane in statistical equilibrium. *J. Atmos. Sci.*, **70**, 1806–1820, doi:10.1175/JAS-D-12-0112.1.
- Cangialosi, J. P., and J. L. Franklin, 2013: 2012 National Hurricane Center Forecast Verification Report. National Hurricane Center, 79 pp. [Available online at http://www.nhc.noaa.gov/verification/pdfs/Verification_2012.pdf.]
- Canuto, V. M., A. Howard, Y. Cheng, and M. S. Dubovikov, 2001: Ocean turbulence. Part I: One-point closure model—Momentum and heat vertical diffusivities. *J. Phys. Oceanogr.*, **31**, 1413–1426, doi:10.1175/1520-0485(2001)031<1413:OTPIOP>2.0.CO;2.
- , —, —, and —, 2002: Ocean turbulence. Part II: Vertical diffusivities of momentum, heat, salt, mass, and passive scalars. *J. Phys. Oceanogr.*, **32**, 240–264, doi:10.1175/1520-0485(2002)032<0240:OTPIVD>2.0.CO;2.
- Chang, S. W., and R. A. Anthes, 1979: The mutual response of the tropical cyclone and the ocean. *J. Phys. Oceanogr.*, **9**, 128–135, doi:10.1175/1520-0485(1979)009<0128:TMROTT>2.0.CO;2.
- Chassignet, E. P., H. E. Hurlburt, O. M. Smedstad, G. R. Halliwell, P. J. Hogan, A. J. Wallcraft, R. Baraille, and R. Bleck, 2007: The HYCOM (HYbrid Coordinate Ocean Model) data assimilative system. *J. Mar. Syst.*, **65**, 60–83, doi:10.1016/j.jmarsys.2005.09.016.
- Cornillon, P., C. Gilman, L. Stramma, O. Brown, R. Evans, and J. Brown, 1987: Processing and analysis of large volumes of satellite-derived thermal infrared data. *J. Geophys. Res.*, **92**, 12 993–13 002, doi:10.1029/JC092iC12p12993.
- D’Asaro, E. A., 2003: The ocean boundary layer below Hurricane Dennis. *J. Phys. Oceanogr.*, **33**, 561–579, doi:10.1175/1520-0485(2003)033<0561:TOBLBH>2.0.CO;2.
- Davis, C., and Coauthors, 2008: Prediction of landfalling hurricanes with the Advanced Hurricane WRF Model. *Mon. Wea. Rev.*, **136**, 1990–2005, doi:10.1175/2007MWR2085.1.
- Dickey, T., and Coauthors, 1998: Upper-ocean temperature response to Hurricane Felix as measured by the Bermuda test-bed mooring. *Mon. Wea. Rev.*, **126**, 1195–1201, doi:10.1175/1520-0493(1998)126<1195:UOTRTH>2.0.CO;2.
- Emanuel, K. A., 1999: Thermodynamic control of hurricane intensity. *Nature*, **401**, 665–669, doi:10.1038/44326.
- , 2003: Tropical cyclones. *Annu. Rev. Earth Planet. Sci.*, **31**, 75–104, doi:10.1146/annurev.earth.31.100901.141259.
- , C. DesAutels, C. Holloway, and R. Korty, 2004: Environmental control of tropical cyclone intensity. *J. Atmos. Sci.*, **61**, 843–858, doi:10.1175/1520-0469(2004)061<0843:ECOTCI>2.0.CO;2.
- Fairall, C. W., E. F. Bradley, D. P. Rogers, J. B. Edson, and G. S. Young, 1996: Bulk parameterization of air–sea fluxes for Tropical Ocean-

- Global Atmosphere Coupled-Ocean Atmosphere Response Experiment. *J. Geophys. Res.*, **101**, 3747, doi:10.1029/95JC03205.
- Fisher, E. L., 1958: Hurricanes and the sea-surface temperature field. *J. Meteor.*, **15**, 328–333, doi:10.1175/1520-0469(1958)015<0328:HATSST>2.0.CO;2.
- Forristall, G. Z., R. C. Hamilton, and V. J. Cardone, 1977: Continental shelf currents in Tropical Storm Delia: Observations and theory. *J. Phys. Oceanogr.*, **7**, 532–546, doi:10.1175/1520-0485(1977)007<0532:CSCITS>2.0.CO;2.
- Fuglister, F. C., and L. V. Worthington, 1951: Some results of a multiple ship survey of the Gulf Stream. *Tellus*, **3**, 1–14, doi:10.1111/j.2153-3490.1951.tb00771.x.
- Garau, B., S. Ruis, W. G. Zhang, A. Pascual, E. Heslop, J. Kerfoot, and J. Tintore, 2011: Thermal lag correction on Slocum CTD glider data. *J. Atmos. Oceanic Technol.*, **28**, 1065–1071, doi:10.1175/JTECH-D-10-05030.1.
- Gentry, M. S., and G. M. Lackmann, 2010: Sensitivity of simulated tropical cyclone structure and intensity to horizontal resolution. *Mon. Wea. Rev.*, **138**, 688–704, doi:10.1175/2009MWR2976.1.
- Glenn, S., and Coauthors, 2016: Stratified coastal ocean interactions with tropical cyclones. *Nat. Commun.*, **7**, 10887, doi:10.1038/ncomms10887.
- , C. Jones, M. Twardowski, L. Bowers, J. Kerfoot, J. Kohut, D. Webb, and O. Schofield, 2008: Glider observations of sediment resuspension in a Middle Atlantic Bight fall transition storm. *Limnol. Oceanogr.*, **53**, 2180–2196, doi:10.4319/lo.2008.53.5_part_2.2180.
- Gould, W. J., and Coauthors, 2004: Argo profiling floats bring new era of in situ ocean observations. *Eos, Trans. Amer. Geophys. Union*, **85**, 185–191, doi:10.1029/2004EO190002.
- Green, B. W., and F. Zhang, 2013: Impacts of air–sea flux parameterizations on the intensity and structure of tropical cyclones. *Mon. Wea. Rev.*, **141**, 2308–2324, doi:10.1175/MWR-D-12-00274.1.
- Haidvogel, D. B., and Coauthors, 2008: Ocean forecasting in terrain-following coordinates: Formulation and skill assessment of the Regional Ocean Modeling System. *J. Comput. Phys.*, **227**, 3595–3624, doi:10.1016/j.jcp.2007.06.016.
- Halliwell, G. R., L. K. Shay, J. K. Brewster, and W. J. Teague, 2011: Evaluation and sensitivity analysis of an ocean model response to Hurricane Ivan. *Mon. Wea. Rev.*, **139**, 921–945, doi:10.1175/2010MWR3104.1.
- Hill, K. A., and G. M. Lackmann, 2009: Analysis of idealized tropical cyclone simulations using the Weather Research and Forecasting Model: Sensitivity to turbulence parameterization and grid spacing. *Mon. Wea. Rev.*, **137**, 745–765, doi:10.1175/2008MWR2220.1.
- Houghton, R. W., R. Schlitz, R. C. Beardsley, B. Butman, and J. L. Chamberlin, 1982: The Middle Atlantic Bight cold pool: Evolution of the temperature structure during summer 1979. *J. Phys. Oceanogr.*, **12**, 1019–1029, doi:10.1175/1520-0485(1982)012<1019:TMABCP>2.0.CO;2.
- Jacob, S. D., and L. K. Shay, 2003: The role of oceanic mesoscale features on the tropical cyclone-induced mixed layer response: A case study. *J. Phys. Oceanogr.*, **33**, 649–676, doi:10.1175/1520-0485(2003)33<649:TROOMF>2.0.CO;2.
- Jaimes, B., and L. K. Shay, 2009: Mixed layer cooling in mesoscale oceanic eddies during Hurricanes Katrina and Rita. *Mon. Wea. Rev.*, **137**, 4188–4207, doi:10.1175/2009MWR2849.1.
- , and —, 2010: Near-inertial wave wake of Hurricanes Katrina and Rita over mesoscale oceanic eddies. *J. Phys. Oceanogr.*, **40**, 1320–1337, doi:10.1175/2010JPO4309.1.
- , and —, 2015: Enhanced wind-driven downwelling flow in warm oceanic eddy features during the intensification of Tropical Cyclone Isaac (2012): Observations and theory. *J. Phys. Oceanogr.*, **45**, 1667–1689, doi:10.1175/JPO-D-14-0176.1.
- , —, and G. R. Halliwell, 2011: The response of quasigeostrophic oceanic vortices to tropical cyclone forcing. *J. Phys. Oceanogr.*, **41**, 1965–1985, doi:10.1175/JPO-D-11-06.1.
- Kain, J. S., 2004: The Kain–Fritsch convective parameterization: An update. *J. Appl. Meteor.*, **43**, 170–181, doi:10.1175/1520-0450(2004)043<0170:TKCPAU>2.0.CO;2.
- Khain, A. P., and I. Ginis, 1991: The mutual response of a moving tropical cyclone and the ocean. *Contrib. Atmos. Phys.*, **64**, 125–141.
- , B. Lynn, and J. Dudhia, 2010: Aerosol effects on intensity of landfalling hurricanes as seen from simulations with the WRF Model with spectral bin microphysics. *J. Atmos. Sci.*, **67**, 365–384, doi:10.1175/2009JAS3210.1.
- , —, and J. Shpund, 2016: High resolution WRF simulations of Hurricane Irene: Sensitivity to aerosols and choice of microphysical schemes. *Atmos. Res.*, **167**, 129–145, doi:10.1016/j.atmosres.2015.07.014.
- Kim, H. S., C. Lozano, V. Tallapragada, D. Iredell, D. Sheinin, H. L. Tolman, V. M. Gerald, and J. Sims, 2014: Performance of ocean simulations in the coupled HWRF-HYCOM model. *J. Atmos. Oceanic Technol.*, **31**, 545–559, doi:10.1175/JTECH-D-13-00013.1.
- Landsea, C. W., and J. L. Franklin, 2013: Atlantic hurricane database uncertainty and presentation of a new database format. *Mon. Wea. Rev.*, **141**, 3576–3592, doi:10.1175/MWR-D-12-00254.1.
- Lee, C.-Y., and S. S. Chen, 2014: Stable boundary layer and its impact on tropical cyclone structure in a coupled atmosphere–ocean model. *Mon. Wea. Rev.*, **142**, 1927–1945, doi:10.1175/MWR-D-13-00122.1.
- Leipper, D. F., 1967: Observed ocean conditions and Hurricane Hilda, 1964. *J. Atmos. Sci.*, **24**, 182–186, doi:10.1175/1520-0469(1967)024<0182:OOCANH>2.0.CO;2.
- Lim, K.-S. S., and S.-Y. Hong, 2010: Development of an effective double-moment cloud microphysics scheme with prognostic cloud condensation nuclei (CCN) for weather and climate models. *Mon. Wea. Rev.*, **138**, 1587–1612, doi:10.1175/2009MWR2968.1.
- Lin, I.-I., C.-H. Chen, I.-F. Pun, W. T. Liu, and C.-C. Wu, 2009: Warm ocean anomaly, air sea fluxes, and the rapid intensification of Tropical Cyclone Nargis (2008). *Geophys. Res. Lett.*, **36**, L03817, doi:10.1029/2008GL035815.
- Liu, B., H. Liu, L. Xie, C. Guan, and D. Zhao, 2011: A coupled atmosphere–wave–ocean modeling system simulation of the intensity of an idealized tropical cyclone. *Mon. Wea. Rev.*, **139**, 132–152, doi:10.1175/2010MWR3396.1.
- Lynn, B. H., and Coauthors, 2016: The sensitivity of Hurricane Irene to aerosols and ocean coupling: Simulations with WRF spectral bin microphysics. *J. Atmos. Sci.*, **73**, 467–486, doi:10.1175/JAS-D-14-0150.1.
- Marks, F. D., and Coauthors, 1998: Landfalling tropical cyclones: Forecast problems and associated research opportunities. *Bull. Amer. Meteor. Soc.*, **79**, 305–323.
- Mayer, D. A., and H. O. Mofjeld, 1981: Near-inertial internal waves observed on the outer shelf in the Middle Atlantic Bight in the wake of Hurricane Belle. *J. Phys. Oceanogr.*, **11**, 87–106, doi:10.1175/1520-0485(1981)011<0087:NIWOO>2.0.CO;2.
- Mehra, A., and I. Rivin, 2010: A real time ocean forecast system for the North Atlantic Ocean. *Terr. Atmos. Oceanic Sci.*, **21**, 211–228, doi:10.3319/TAO.2009.04.16.01(IWNOF).
- Mei, W., C. Pasquero, and F. Primeau, 2012: The effect of translation speed upon the intensity of tropical cyclones over the tropical ocean. *Geophys. Res. Lett.*, **39**, L07801, doi:10.1029/2011GL050765.

- Mesinger, F., and Coauthors, 2006: North American Regional Reanalysis. *Bull. Amer. Meteor. Soc.*, **87**, 343–360, doi:[10.1175/BAMS-87-3-343](https://doi.org/10.1175/BAMS-87-3-343).
- Miles, T., S. Glenn, and O. Schofield, 2013: Temporal and spatial variability in fall storm induced sediment resuspension on the Mid-Atlantic Bight. *Cont. Shelf Res.*, **63**, S36–S49, doi:[10.1016/j.csr.2012.08.006](https://doi.org/10.1016/j.csr.2012.08.006).
- , G. N. Seroka, J. T. Kohut, O. Schofield, and S. M. Glenn, 2015: Glider observations and modeling of sediment transport in Hurricane Sandy. *J. Geophys. Res. Ocean*, **120**, 1771–1791, doi:[10.1002/2014JC010474](https://doi.org/10.1002/2014JC010474).
- Pollard, R. T., P. B. Rhines, and R. O. Thompson, 1972: The deepening of the wind-mixed layer. *Geophys. Astrophys. Fluid Dyn.*, **4**, 381–404, doi:[10.1080/03091927208236105](https://doi.org/10.1080/03091927208236105).
- Price, J. F., 1981: Upper ocean response to a hurricane. *J. Phys. Oceanogr.*, **11**, 153–175, doi:[10.1175/1520-0485\(1981\)011<0153:UORTAH>2.0.CO;2](https://doi.org/10.1175/1520-0485(1981)011<0153:UORTAH>2.0.CO;2).
- , R. A. Weller, and R. Pinkel, 1986: Diurnal cycling: Observations and models of the upper ocean response to diurnal heating, cooling, and wind mixing. *J. Geophys. Res.*, **91**, 8411–8427, doi:[10.1029/JC091iC07p08411](https://doi.org/10.1029/JC091iC07p08411).
- , T. B. Sanford, and G. Z. Forristall, 1994: Forced stage response to a moving hurricane. *J. Phys. Oceanogr.*, **24**, 233–260, doi:[10.1175/1520-0485\(1994\)024<0233:FSRTAM>2.0.CO;2](https://doi.org/10.1175/1520-0485(1994)024<0233:FSRTAM>2.0.CO;2).
- Rappaport, E. N., J. L. Frankling, M. DeMaria, L. K. Shay, and E. J. Gibney, 2010: Tropical cyclone intensity change before U.S. Gulf Coast landfall. *Wea. Forecasting*, **25**, 1380–1396, doi:[10.1175/2010WAF2222369.1](https://doi.org/10.1175/2010WAF2222369.1).
- Reynolds, R. W., and D. B. Chelton, 2010: Comparisons of daily sea surface temperature analyses for 2007–08. *J. Climate*, **23**, 3545–3562, doi:[10.1175/2010JCLI3294.1](https://doi.org/10.1175/2010JCLI3294.1).
- Rheme, J. R., C. A. Sisko, and R. D. Knabb, 2006: On the calculation of vertical shear: An operational perspective. *27th Conf. on Hurricanes and Tropical Meteorology*, Monterey, CA, Amer. Meteor. Soc., 14A.4. [Available online at https://ams.confex.com/ams/27Hurricanes/techprogram/paper_108724.htm.]
- Roemmich, D., and Coauthors, 2009: The Argo Program: Observing the global ocean with profiling floats. *Oceanography*, **22**, 34–43, doi:[10.5670/oceanog.2009.36](https://doi.org/10.5670/oceanog.2009.36).
- Ruiz, S., L. Renault, B. Garau, and J. Tintoré, 2012: Underwater glider observations and modeling of an abrupt mixing event in the upper ocean. *Geophys. Res. Lett.*, **39**, L01603, doi:[10.1029/2011GL050078](https://doi.org/10.1029/2011GL050078).
- Sampson, C. R., and A. J. Schrader, 2000: The Automated Tropical Cyclone Forecasting System (version 3.2). *Bull. Amer. Meteor. Soc.*, **81**, 1231–1240, doi:[10.1175/1520-0477\(2000\)081<1231:TATCFS>2.3.CO;2](https://doi.org/10.1175/1520-0477(2000)081<1231:TATCFS>2.3.CO;2).
- Sanabia, E. R., and S. R. Jayne, 2014: Evolution of the upper-ocean thermal structure beneath Hurricanes Iselle and Julio (2014). *2014 Fall Meeting*, San Francisco, CA, Amer. Geophys. Union, Abstract A11O-07.
- , B. S. Barrett, P. G. Black, S. Chen, and J. A. Cummings, 2013: Real-time upper-ocean temperature observations from aircraft during operational hurricane reconnaissance missions: AXBT demonstration project year one results. *Wea. Forecasting*, **28**, 1404–1422, doi:[10.1175/WAF-D-12-00107.1](https://doi.org/10.1175/WAF-D-12-00107.1).
- , S. R. Jayne, W. Swick, S. Chen, and J. Cummings, 2016: Variability in upper-ocean thermal structure beneath tropical cyclones as observed by air-deployed profiling floats. *32nd Conf. on Hurricanes and Tropical Meteorology*, San Juan, Puerto Rico, Amer. Meteor. Soc., 3B.4. [Available online at <https://ams.confex.com/ams/32Hurr/webprogram/Paper293996.html>.]
- Sanford, T. B., P. G. Black, J. R. Haustein, J. W. Feeney, G. Z. Forristall, and J. F. Price, 1987: Ocean response to a hurricane. Part I: Observations. *J. Phys. Oceanogr.*, **17**, 2065–2083, doi:[10.1175/1520-0485\(1987\)017<2065:ORTAHP>2.0.CO;2](https://doi.org/10.1175/1520-0485(1987)017<2065:ORTAHP>2.0.CO;2).
- Schade, L. R., and K. A. Emanuel, 1999: The ocean's effect on the intensity of tropical cyclones: Results from a simple coupled atmosphere–ocean model. *J. Atmos. Sci.*, **56**, 642–651, doi:[10.1175/1520-0469\(1999\)056<0642:TOSEOT>2.0.CO;2](https://doi.org/10.1175/1520-0469(1999)056<0642:TOSEOT>2.0.CO;2).
- Schofield, O., and Coauthors, 2007: Slocum gliders: Robust and ready. *J. F. Robot.*, **24**, 473–485, doi:[10.1002/rob.20200](https://doi.org/10.1002/rob.20200).
- Sessions, M. H., T. P. Barnett, and W. S. Wilson, 1976: The airborne expendable bathythermograph. *Deep-Sea Res. Oceanogr. Abstr.*, **23**, 779–782, doi:[10.1016/S0011-7471\(76\)80021-6](https://doi.org/10.1016/S0011-7471(76)80021-6).
- Shay, L. K., P. G. Black, A. J. Mariano, J. D. Hawkins, and R. L. Elsberry, 1992: Upper ocean response to Hurricane Gilbert. *J. Geophys. Res.*, **97**, 20 227–20 248, doi:[10.1029/92JC01586](https://doi.org/10.1029/92JC01586).
- Skamarock, W. C., and Coauthors, 2008: A description of the Advanced Research WRF version 3. NCAR Tech. Note NCAR/TN-475+STR, 113 pp., doi:[10.5065/D68S4MVH](https://doi.org/10.5065/D68S4MVH).
- Suda, K., 1943: *Ocean Science*. Kokin-Shoin, 770 pp.
- Sutyryn, G. G., and E. A. Agrenich, 1979: Interaction of the boundary layers of the ocean and atmosphere in a tropical cyclone. *Meteor. Gidrol.*, **2**, 45–56.
- , and A. P. Khain, 1984: Effect of the ocean–atmosphere interaction on the intensity of a moving tropical cyclone. *Atmos. Oceanic Phys.*, **20**, 697–703.
- Tallapragada, V., and Coauthors, 2011: Hurricane Weather Research and Forecasting (HWRF) model: 2011 scientific documentation. Developmental Testbed Center, 81 pp. [Available online at http://www.dtcenter.org/HurrWRF/users/docs/scientific_documents/HWRFScientificDocumentation_August2011.pdf.]
- Torn, R. D., and C. Snyder, 2012: Uncertainty of tropical cyclone best-track information. *Wea. Forecasting*, **27**, 715–729, doi:[10.1175/WAF-D-11-00085.1](https://doi.org/10.1175/WAF-D-11-00085.1).
- Walker, N. D., R. R. Leben, and S. Balasubramanian, 2005: Hurricane-forced upwelling and chlorophyll α enhancement within cold-core cyclones in the Gulf of Mexico. *Geophys. Res. Lett.*, **32**, L18610, doi:[10.1029/2005GL023716](https://doi.org/10.1029/2005GL023716).
- Wilkin, J. L., and E. J. Hunter, 2013: An assessment of the skill of real-time models of Mid-Atlantic Bight continental shelf circulation. *J. Geophys. Res. Ocean*, **118**, 2919–2933, doi:[10.1002/jgrc.20223](https://doi.org/10.1002/jgrc.20223).
- Zambon, J. B., R. He, and J. C. Warner, 2014a: Investigation of Hurricane Ivan using the Coupled Ocean–Atmosphere–Wave–Sediment Transport (COAWST) model. *Ocean Dyn.*, **64**, 1535–1554, doi:[10.1007/s10236-014-0777-7](https://doi.org/10.1007/s10236-014-0777-7).
- , —, and —, 2014b: Tropical to extratropical: Marine environmental changes associated with Superstorm Sandy prior to its landfall. *Geophys. Res. Lett.*, **41**, 8935–8943, doi:[10.1002/2014GL061357](https://doi.org/10.1002/2014GL061357).